Chapter 6
Evolution and Nucleosynthesis of Very Massive Stars

Raphael Hirschi

Abstract In this chapter, after a brief introduction and overview of stellar evolution, we discuss the evolution and nucleosynthesis of very massive stars (VMS: $M > 100\,M_{\odot}$) in the context of recent stellar evolution model calculations. This chapter covers the following aspects: general properties, evolution of surface properties, late central evolution, and nucleosynthesis including their dependence on metallicity, mass loss and rotation. Since very massive stars have very large convective cores during the main-sequence phase, their evolution is not so much affected by rotational mixing, but more by mass loss through stellar winds. Their evolution is never far from a homogeneous evolution even without rotational mixing. All VMS at metallicities close to solar end their life as WC(-WO) type Wolf-Rayet stars. Due to very important mass loss through stellar winds, these stars may have luminosities during the advanced phases of their evolution similar to stars with initial masses between 60 and $120\,M_{\odot}$. A distinctive feature which may be used to disentangle Wolf-Rayet stars originating from VMS from those originating from lower initial masses is the enhanced abundances of neon and magnesium at the surface of WC stars. At solar metallicity, mass loss is so strong that even if a star is born with several hundred solar masses, it will end its life with less than $50\,M_{\odot}$ (using current mass loss prescriptions). At the metallicity of the LMC and lower, on the other hand, mass loss is weaker and might enable stars to undergo pair-instability supernovae.

6.1 Introduction

For a long time, the evolution of VMS was considered only in the framework of Pop III stars. Indeed, it was expected that, only in metal free environments, could such massive stars be formed, since the absence of dust, an efficient cooling agent, would prevent a strong fragmentation of the proto-stellar cloud (Bromm et al. 1999;

R. Hirschi (✉)
Astrophysics, Lennard-Jones Labs 2.09, EPSAM, Keele University, ST5 5BG, Staffordshire, UK

Kavli Institute for the Physics and Mathematics of the Universe (WPI), University of Tokyo, 5-1-5 Kashiwanoha, Kashiwa, 277-8583, Japan
e-mail: r.hirschi@keele.ac.uk

J.S. Vink (ed.), *Very Massive Stars in the Local Universe*, Astrophysics and Space Science Library 412, DOI 10.1007/978-3-319-09596-7_6

Abel et al. 2002).[1] It came therefore as a surprise when it was discovered that the most metal-poor low-mass stars, likely formed from a mixture between the ejecta of these Pop III stars and pristine interstellar medium, did not show any signature of the peculiar nucleosynthesis of the VMS (Heger and Woosley 2002; Umeda and Nomoto 2002; Christlieb et al. 2002; Frebel et al. 2005). While such observations cannot rule out the existence of these VMS in Pop III generations (their nucleosynthetic signature may have been erased by the more important impact of stars in other mass ranges), it seriously questions the importance of such object for understanding the early chemical evolution of galaxies. Ironically, when the importance of VMS in the context of the first stellar generations fades, they appear as potentially interesting objects in the framework of present day stellar populations.

For a long time, observations favored a present-day upper mass limit for stars around 150 $M_{\odot}$ (Figer 2005; Oey and Clarke 2005). Recently, however, Crowther et al. (2010) have re-assessed the properties of the brightest members of the R136a star cluster, revealing exceptionally high luminosities (see Chaps. 1 and 2 for more details). The comparison between main sequence evolutionary models for rotating and non-rotating stars and observed spectra resulted in high current ($\leq$265 $M_{\odot}$) and initial ($\leq$320 $M_{\odot}$) masses for these stars. The formation scenarios for these VMS are presented in Chap. 3.

The above observations triggered a new interest in the evolution of very massive stars. However, since VMS are so rare, only a few of them are known and we have to rely on stellar evolution models in order to study their properties and evolution. In this chapter, the evolution of VMS will be discussed based on stellar evolution models calculated using the Geneva stellar evolution code (Eggenberger et al. 2007) including the modifications implemented to follow the advanced stages as described in Hirschi et al. (2004a). Models at solar ($Z = 0.014$), Large Magellanic Cloud (LMC, $Z = 0.006$) and Small Magellanic Cloud (SMC, $Z = 0.002$) metallicities will be presented (see Yusof et al. 2013, for full details about these models). These models will also be compared to models of normal massive stars calculated with the same input physics at solar metallicity ($Z = 0.014$) presented in Ekström et al. (2012) and Georgy et al. (2012) as well as their extension to lower metallicities (Georgy et al. 2013).

In Sect. 6.2, we review the basics of stellar evolution models and their key physical ingredients. The general properties and early evolution of VMS are presented in Sect. 6.3. The Wolf-Rayet stars originating from VMS are discussed in Sect. 6.4. The late evolution and possible fates of the VMS is the subject of Sect. 6.5. The nucleosynthesis and contribution to chemical evolution of galaxies is discussed in Sect. 6.6. A summary and conclusions are given in section "Summary and Conclusion".

[1]Note, however, that recent star formation simulations find lower-mass stars forming in groups, similarly to present-day star formation (Stacy et al. 2010; Greif et al. 2010).

6.2 Stellar Evolution Models

The evolution of VMS is similar enough to more common massive stars that the same stellar evolution codes can be used to study their evolution and corresponding nucleosynthesis. Stellar evolution models require a wide range of input physics ranging from nuclear reaction rates to mass loss prescriptions. In this section, we review the basic equations that govern the structure and evolution of stars as well as some of the key input physics with a special emphasis on mass loss, rotation and magnetic fields.

6.2.1 Stellar Structure Equations

There are four equations describing the evolution of the structure of stars: the mass, momentum and energy conservation equations and the energy transport equations, which we recall below. On top of that, the equations of the evolution of chemical elements abundances are to be followed. These equations are discussed in the next section. In the Geneva stellar evolution code (GENEC, see Eggenberger et al. 2007), which we base our presentation on in this section, the problem is treated in one dimension (1D) and the equations of the evolution of chemical elements abundances are calculated separately from the structure equations, as in the original version of Kippenhahn and Weigert (Kippenhahn et al. 1967; Kippenhahn and Weigert 1990). In GENEC, rotation is included and spherical symmetry is no longer assumed. The effective gravity (sum of the centrifugal force and gravity) can in fact no longer be derived from a potential and the case is said to be non–conservative. The problem can still be treated in 1D by assuming that the angular velocity is constant on isobars. This assumes that there is a strong horizontal (along isobars) turbulence which enforces constant angular velocity on isobars (Zahn 1992). The case is referred to as "shellular" rotation and using reasonable simplifications described in Meynet and Maeder (1997), the usual set of four structure equations (as used for non-rotating stellar models) can be recovered:

- Energy conservation:

$$\frac{\partial L_P}{\partial M_P} = \epsilon_{nucl} - \epsilon_\nu + \epsilon_{grav} = \epsilon_{nucl} - \epsilon_\nu - c_P \frac{\partial \overline{T}}{\partial t} + \frac{\delta}{\overline{\rho}} \frac{\partial P}{\partial t} \tag{6.1}$$

  Where L_P is the luminosity, M_P the Lagrangian mass coordinate, and ϵ_{nucl}, ϵ_ν, and ϵ_{grav} are the energy generation rates per unit mass for nuclear reactions, neutrinos and gravitational energy changes due to contraction or expansion, respectively. T is the temperature, c_P the specific heat at constant pressure, t the time, P the pressure, ρ the density and $\delta = -\partial \ln \rho / \partial \ln T$.

- Momentum equation:

$$\frac{\partial P}{\partial M_P} = -\frac{GM_P}{4\pi r_P^4} f_P \tag{6.2}$$

  Where r_P is the radius of the shell enclosing mass M_P and G the gravitational constant.
- Mass conservation (continuity equation):

$$\frac{\partial r_P}{\partial M_P} = \frac{1}{4\pi r_P^2 \overline{\rho}} \tag{6.3}$$

- Energy transport equation:

$$\frac{\partial \ln \overline{T}}{\partial M_P} = -\frac{GM_P}{4\pi r_P^4 P} f_P \min[\nabla_{\rm ad}, \nabla_{\rm rad} \frac{f_T}{f_P}] \tag{6.4}$$

where

$$\nabla_{\rm ad} = \left(\frac{\partial \ln \overline{T}}{\partial \ln P}\right)_{\rm ad} = \frac{P\delta}{\overline{T}\overline{\rho}c_P} \quad \text{(convective zones)},$$

$$\nabla_{\rm rad} = \frac{3}{64\pi\sigma G}\frac{\kappa L_P P}{M_P \overline{T}^4} \quad \text{(radiative zones)},$$

where κ is the total opacity and σ is the Stefan-Boltzmann constant.

$$f_P = \frac{4\pi r_P^4}{GM_P S_P}\frac{1}{< g^{-1} >},$$

$$f_T = \left(\frac{4\pi r_P^2}{S_P}\right)^2 \frac{1}{< g >< g^{-1} >},$$

$< x >$ is x averaged on an isobaric surface, $\overline{x}$ is x averaged in the volume separating two successive isobars and the index P refers to the isobar with a pressure equal to P. g is the effective gravity and S_P is the surface of the isobar (see Meynet and Maeder 1997, for more details). The implementation of the structure equations into other stellar evolution codes are presented for example in Paxton et al. (2011) and Chieffi et al. (1998).

6.2.2 Mass Loss

Mass loss strongly affects the evolution of very massive stars as we shall describe below. Mass loss is already discussed in Chap. 4 but here we will recall the different mass loss prescriptions used in stellar evolution calculations and how they relate to each other. In the models presented in this chapter, the following prescriptions were used. For main-sequence stars, the prescription for radiative line driven winds from Vink et al. (2001a) was used, which compare rather well with observations (Crowther et al. 2010; Muijres et al. 2011). For stars in a domain not covered by the Vink et al. prescription, the de Jager et al. (1988a) prescription was applied to models with $\log(T_{\rm eff}) > 3.7$. For $\log(T_{\rm eff}) \leq 3.7$, a linear fit to the data from Sylvester et al. (1998) and van Loon et al. (1999) (see Crowther 2001) was performed. The formula used is given in Eq. 2.1 in Bennett et al. (2012).

In the stellar evolution simulations, the stellar wind is not simulated self-consistently and a criterion is used to determine when a star becomes a WR star. Usually, a star becomes a WR when the surface hydrogen mass fraction, X_s, becomes inferior to 0.3 (sometimes when it is inferior to 0.4) and the effective temperature, $\log(T_{\rm eff})$, is greater than 4.0. The mass loss rate used during the WR phase depends on the WR sub-type. For the eWNL phase (when $0.3 > X_s > 0.05$), the Gräfener and Hamann (2008) recipe was used (in the validity domain of this prescription, which usually covers most of the eWNL phase). In many cases, the WR mass-loss rate of Gräfener and Hamann (2008) is lower than the rate of Vink et al. (2001a), in which case, the latter was used. For the eWNE phase – when $0.05 > X_s$ and the ratio of the mass fractions of $(^{12}\mathrm{C} + {}^{16}\mathrm{O})/{}^{4}\mathrm{He} < 0.03$ – and WC/WO phases – when $(^{12}\mathrm{C} + {}^{16}\mathrm{O})/{}^{4}\mathrm{He} > 0.03$ – the corresponding prescriptions of Nugis and Lamers (2000a) were used. Note also that both the Nugis and Lamers (2000a) and Gräfener and Hamann (2008) mass-loss rates account for clumping effects (Muijres et al. 2011).

As is discussed below, the mass loss rates from Nugis and Lamers (2000a) for the eWNE phase are much larger than in other phases and thus the largest mass loss occurs during this phase. In Crowther et al. (2010), the mass loss prescription from Nugis and Lamers (2000a) was used for both the eWNL and eWNE phases (with a clumping factor, $f = 0.1$). The models presented in this chapter thus lose less mass than those presented in Crowther et al. (2010) during the eWNL phase.

The metallicity dependence of the mass loss rates is commonly included in the following way. The mass loss rate used at a given metallicity, $\dot{M}(Z)$, is the mass loss rate at solar metallicity, $\dot{M}(Z_\odot)$, multiplied by the ratio of the metallicities to the power of α: $\dot{M}(Z) = \dot{M}(Z_\odot)(Z/Z_\odot)^\alpha$. α was set to 0.85 for the O-type phase and WN phase and 0.66 for the WC and WO phases; and for WR stars the initial metallicity rather than the actual surface metallicity was used in the equation above following Eldridge and Vink (2006). α was set to 0.5 for the de Jager et al. (1988a) prescription.

For rotating models, the correction factor described below in Eq. 6.5 is applied to the radiative mass-loss rate.

6.2.3 Rotation and Magnetic Mields

The physics of rotation included in stellar evolution codes has been developed extensively over the last 20 years. A recent review of this development can be found in Maeder and Meynet (2012). The effects induced by rotation can be divided into three categories.

1. **Hydrostatic effects**: The centrifugal force changes the hydrostatic equilibrium of the star. The star becomes oblate and the equations describing the stellar structure have to be modified as described above.
2. **Mass loss enhancement and anisotropy**: Mass loss depends on the opacity and the effective gravity (sum of gravity and centrifugal force) at the surface. The larger the opacity, the larger the mass loss. The higher the effective gravity, the higher the radiative flux (von Zeipel 1924) and effective temperature. Rotation, via the centrifugal force, reduces the surface effective gravity at the equator compared to the pole. As a result, the radiative flux of the star is larger at the pole than at the equator. In massive hot stars, since the opacity is dominated by the temperature–independent electron scattering, rotation enhances mass loss at the pole. If the opacity increases when the temperature decreases (in cooler stars), mass loss can be enhanced at the equator when the bi-stability is reached (see mass loss chapter for more details).

For rotating models, the mass loss rates can be obtained by applying a correction factor to the radiative mass loss rate as described in Maeder and Meynet (2000):

$$\dot{M}(\Omega) = F_\Omega \cdot \dot{M}(\Omega = 0) = F_\Omega \cdot \dot{M}_{\rm rad}$$
$$\text{with} \quad F_\Omega = \frac{(1-\Gamma)^{\frac{1}{\alpha}-1}}{\left[1 - \frac{\Omega^2}{2\pi G \rho_{\rm m}} - \Gamma\right]^{\frac{1}{\alpha}-1}} \tag{6.5}$$

where $\Gamma = L/L_{\rm Edd} = \kappa L/(4\pi cGM)$ is the Eddington factor (with κ the total opacity), and α the $T_{\rm eff}$−dependent force multiplier parameter. Enhancement factors (F_Ω) are generally close to one but they may become very large when $\Gamma \gtrsim 0.7$ or $\Omega/\Omega_{\rm crit} > 0.9$ (see Maeder and Meynet 2000; Georgy et al. 2011, for more details). If critical rotation, where the centrifugal force balances gravity at the equator, is reached, mechanical mass loss may occur and produce a decretion disk (see Krtička et al. 2011, for more details). In most stellar evolution codes, the mass loss is artificially enhanced when $\Omega/\Omega_{\rm crit} \gtrsim 0.95$ to ensure that the ratio does not become larger than unity but multi-dimensional simulations are required to provide new prescriptions to use in stellar evolution codes.

For mass loss rates, $\dot{M}(\Omega = 0)$, the following prescriptions are commonly used: Vink et al. (2001b) for radiatively driven wind of O-type stars, Nugis and Lamers (2000b) for Wolf-Rayet stars and de Jager et al. (1988b) for cooler stars not covered by the other two prescriptions and for which dust and pulsation could play a role in the driving of the wind.

3. **Rotation driven instabilities**: The main rotation driven instabilities are horizontal turbulence, meridional circulation and dynamical and secular shear (see Maeder 2009, for a comprehensive description of rotation-induced instabilities).

Horizontal turbulence corresponds to turbulence along the isobars. If this turbulence is strong, rotation is constant on isobars and the situation is usually referred to as "shellular rotation" (Zahn 1992). The horizontal turbulence is expected to be stronger than the vertical turbulence because there is no restoring buoyancy force along isobars (see Maeder 2003, for recent development on this topic).

Meridional circulation, also referred to as Eddington–Sweet circulation, arises from the local breakdown of radiative equilibrium in rotating stars. This is due to the fact that surfaces of constant temperature do not coincide with surfaces of constant pressure. Indeed, since rotation elongates isobars at the equator, the temperature on the same isobar is lower at the equator than at the pole. This induces large scale circulation of matter, in which matter usually rises at the pole and descends at the equator (see Fig. 6.1).

In this situation, angular momentum is transported inwards. It is however also possible for the circulation to go in the reverse direction and, in this second case, angular momentum is transported outwards. Circulation corresponds to an advective process, which is different from diffusion because the latter can only erode gradients. Advection can either build or erode angular velocity gradients (see Maeder and Zahn 1998, for more details).

Dynamical shear occurs when the excess energy contained in differentially rotating layers is larger then the work that needs to be done to overcome the buoyancy force. The criterion for stability against dynamical shear instability is the

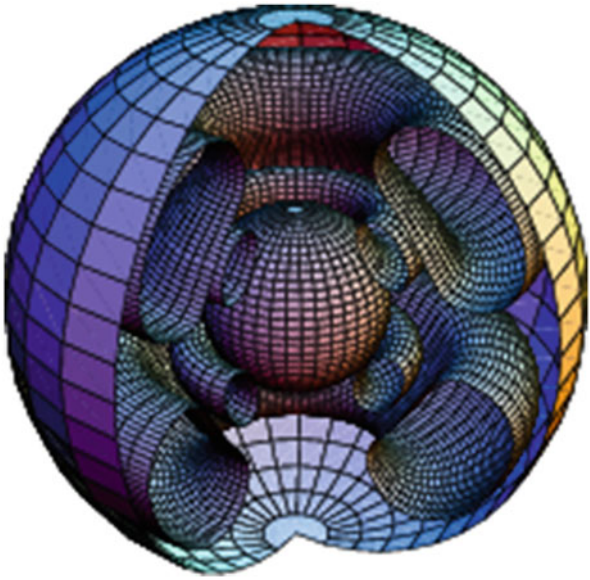

Fig. 6.1 Streamlines of meridional circulation in a rotating $20\,M_\odot$ model with solar metallicity and $v_{\rm ini} = 300\,{\rm km\,s^{-1}}$ at the beginning of the H–burning phase. The streamlines are in the meridian plane. In the upper hemisphere on the right section, matter is turning counterclockwise along the outer streamline and clockwise along the inner one. The outer sphere is the star surface and has a radius equal to $5.2\,R_\odot$. The inner sphere is the outer boundary of the convective core. It has a radius of $1.7\,R_\odot$ (Illustration from Meynet and Maeder 2002)

Richardson criterion:

$$Ri = \frac{N^2}{(\partial U/\partial z)^2} > \frac{1}{4} = Ri_c, \tag{6.6}$$

where U is the horizontal velocity, z the vertical coordinate and N^2 the Brunt–Väisälä frequency.

The critical value of the Richardson criterion, $Ri_c = 1/4$, corresponds to the situation where the excess kinetic energy contained in the differentially rotating layers is equal to the work done against the restoring force of the density gradient (also called buoyancy force). It is therefore used by most authors as the limit for the occurrence of the dynamical shear. However, studies by Canuto (2002) show that turbulence may occur as long as $Ri \lesssim Ri_c \sim 1$. This critical value is consistent with numerical simulations done by Brüggen and Hillebrandt (2001) where they find shear mixing for values of Ri greater than $1/4$ (up to about 1.5).

Different dynamical shear diffusion coefficients, D, can be found in the literature. The one used in GENEC is:

$$D = \frac{1}{3} vl = \frac{1}{3} \frac{v}{l} l^2 = \frac{1}{3} r \frac{\mathrm{d}\,\Omega}{\mathrm{d}\,r} \Delta r^2 = \frac{1}{3} r \Delta\Omega \, \Delta r \tag{6.7}$$

where r is the mean radius of the zone where the instability occurs, $\Delta\Omega$ is the variation of Ω over this zone and Δr is the extent of the zone. The zone is the reunion of consecutive shells where $Ri < Ri_c$ (see Hirschi et al. 2004b, for more details and references).

If the differential rotation is not strong enough to induce dynamical shear, it can still induce the secular shear instability when thermal turbulence reduces the effect of the buoyancy force. The secular shear instability occurs therefore on the thermal time scale, which is much longer than the dynamical one. Note that the way the inhibiting effect of the molecular weight (μ) gradients on secular shear is taken into account impacts strongly the efficiency of the shear. In some work, the inhibiting effect of μ–gradients is so strong that secular shear is suppressed below a certain threshold value of differential rotation (Heger et al. 2000). In other work (Maeder 1997), thermal instabilities and horizontal turbulence reduce the inhibiting effect of the μ–gradients. As a result, shear is not suppressed below a threshold value of differential rotation but only decreased when μ–gradients are present.

There are other minor instabilities induced by rotation: the GSF instability (Goldreich and Schubert 1967; Fricke 1968; Hirschi and Maeder 2010), the ABCD instability (Knobloch and Spruit 1983; Heger et al. 2000) and the Solberg–Høiland instability (Kippenhahn and Weigert 1990). The GSF instability is induced by axisymmetric perturbations. The ABCD instability is a kind of horizontal convection. Finally, Solberg–Høiland stability criterion is the criterion that should be used instead of the Ledoux or Schwarzschild criterion in rotating stars. However, including the dynamical shear instability also takes into account the Solberg–Høiland instability (Hirschi et al. 2004b).

Transport of Angular Momentum

For shellular rotation, the equation of transport of angular momentum (Zahn 1992) in the vertical direction is (in lagrangian coordinates):

$$\rho \frac{d}{dt}\left(r^2\Omega\right)_{M_r} = \frac{1}{5r^2}\frac{\partial}{\partial r}\left(\rho r^4 \Omega U(r)\right) + \frac{1}{r^2}\frac{\partial}{\partial r}\left(\rho D r^4 \frac{\partial \Omega}{\partial r}\right) , \tag{6.8}$$

where $\Omega(r)$ is the mean angular velocity at level r, $U(r)$ the vertical component of the meridional circulation velocity and D the diffusion coefficient due to the sum of the various turbulent diffusion processes (convection, shears and other rotation induced instabilities apart from meridional circulation). Note that angular momentum is conserved in the case of contraction or expansion. The first term on the right hand side, corresponding to meridional circulation, is an *advective* term. The second term on the right hand side, which corresponds to the diffusion processes, is a *diffusive* term. The correct treatment of advection is very costly numerically because Eq. 6.8 is a fourth order equation (the expression of $U(r)$ contains third order derivatives of Ω, see Zahn 1992). This is why some research groups treat meridional circulation in a diffusive way (see for example Heger et al. 2000) with the risk of transporting angular momentum in the wrong direction (in the case meridional circulation builds gradients).

Transport of Chemical Species

The transport of chemical elements is also governed by a diffusion–advection equation like Eq. 6.8. However, if the horizontal component of the turbulent diffusion is large, the vertical advection of the elements (but not that of the angular momentum) can be treated as a simple diffusion (Chaboyer and Zahn 1992) with a diffusion coefficient $D_{\rm eff}$,

$$D_{\rm eff} = \frac{\mid rU(r) \mid^2}{30 D_h} , \tag{6.9}$$

where D_h is the coefficient of horizontal turbulence (Zahn 1992). Equation 6.9 expresses that the vertical advection of chemical elements is severely inhibited by the strong horizontal turbulence characterized by D_h. The change of the mass fraction X_i of the chemical species i is simply

$$\left(\frac{dX_i}{dt}\right)_{M_r} = \left(\frac{\partial}{\partial M_r}\right)_t \left[(4\pi r^2 \rho)^2 D_{\rm mix}\left(\frac{\partial X_i}{\partial M_r}\right)_t\right] + \left(\frac{dX_i}{dt}\right)_{\rm nuclear} , \tag{6.10}$$

where the second term on the right accounts for composition changes due to nuclear reactions. The coefficient $D_{\rm mix}$ is the sum $D_{\rm mix} = D + D_{\rm eff}$, where D is the term

appearing in Eq. 6.8 and $D_{\rm eff}$ accounts for the combined effect of advection and horizontal turbulence.

Interaction Between Rotation and Magnetic Fields

Circular spectro-polarimetric surveys have obtained evidence for the presence of magnetic field at the surface of OB stars (see e.g. the review by Walder et al. 2011, and references therein). The origin of these magnetic fields is still unknown. It might be fossil fields or fields produced through a dynamo mechanism.

The central question for the evolution of massive stars is whether a dynamo is at work in internal radiative zones. This could have far reaching consequences concerning the mixing of the elements and the loss of angular momentum. In particular, the interaction between rotation and magnetic fields in the stellar interior strongly affects the angular momentum retained in the core and thus the initial rotation rate of pulsars and which massive stars could die as long & soft gamma-ray bursts (GRBs), see Vink et al. (2011a) and the discussion in Sect. 6 in Georgy et al. (2012, and references therein).

The interplay between rotation and magnetic field has been studied in stellar evolution calculations using the Tayler–Spruit dynamo (Spruit 2002; Maeder and Meynet 2005). Some numerical simulations confirm the existence of a magnetic instability, however the existence of the dynamo is still controversial (Braithwaite 2006; Zahn et al. 2007).

The Tayler-Spruit dynamo is based on the fact that a purely toroidal field $B_\varphi(r, \vartheta)$, even very weak, in a stable stratified star is unstable on an Alfvén timescale $1/\omega_{\rm A}$. This is the first magnetic instability to appear. It is non–axisymmetric of type $m = 1$ (Spruit 2002), occurs under a wide range of conditions and is characterized by a low threshold and a short growth time. In a rotating star, the instability is also present, however the growth rate $\sigma_{\rm B}$ of the instability is, if $\omega_{\rm A} \ll \Omega$,

$$\sigma_{\rm B} = \frac{\omega_{\rm A}^2}{\Omega}\,, \tag{6.11}$$

instead of the Alfvén frequency $\omega_{\rm A}$, because the growth rate of the instability is reduced by the Coriolis force (Spruit 2002). One usually has the following ordering of the different frequencies, $N \gg \Omega \gg \omega_{\rm A}$. In the Sun, one has $N \approx 10^{-3}\,{\rm s}^{-1}$, $\Omega = 3 \times 10^{-6}\,{\rm s}^{-1}$ and a field of 1 kG would give an Alfvén frequency as low as $\omega_{\rm A} = 4 \times 10^{-9}\,{\rm s}^{-1}$ (where N^2 is the Brunt–Väisälä frequency).

This theory enables us to establish the two quantities that we are mainly interested in for stellar evolution: the magnetic viscosity ν, which expresses the mechanical coupling due to the magnetic field $\mathbf{B}$, and the magnetic diffusivity η, which expresses the transport by a magnetic instability and thus also the damping of the instability. The parameter η also expresses the vertical transport of the chemical elements and enters Eq. 6.10, while the viscosity ν determines the vertical transport

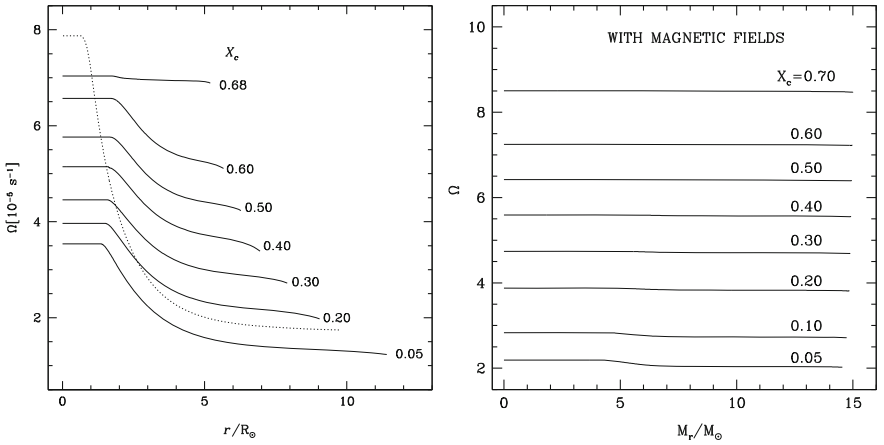

Fig. 6.2 *Left*: evolution of the angular velocity Ω as a function of the distance to the center in a 20 $M_\odot$ star with $v_{\rm ini} = 300\,{\rm km\,s^{-1}}$. X_c is the hydrogen mass fraction at the center. The *dotted line* shows the profile when the He–core contracts at the end of the H–burning phase. *Right*: rotation profiles at various stages of evolution (labelled by the central H content X_c) of a 15 $M_\odot$ model with $X = 0.705$, $Z = 0.02$, an initial velocity of 300 km s^{-1} and magnetic field from the Tayler–Spruit dynamo (Taken from Maeder and Meynet (2005))

of the angular momentum by the magnetic field and enters the second term on the right-hand side of Eq. 6.8.

Figure 6.2 shows the differences in the internal Ω–profiles during the evolution of a 20 $M_\odot$ star with and without magnetic field created by the Tayler–Spruit dynamo. Without magnetic field, the star has a significant differential rotation, while Ω is almost constant when a magnetic field created by the dynamo is present. It is not perfectly constant, otherwise there would be no dynamo. In fact, the rotation rapidly adjusts itself to the minimum differential rotation necessary to sustain the dynamo. One could then assume that the mixing of chemical elements is suppressed by magnetic fields. This is, however, not the case since the interplay between magnetic fields and the meridional circulation tend to lead to more mixing in models including magnetic fields compared to models not including magnetic fields (Maeder and Meynet 2005). Fast rotating models of GRB progenitors calculated by Yoon et al. (2006) also experience a strong chemical internal mixing leading to the stars undergoing quasi-chemical homogeneous evolution. The study of the interaction between rotation and magnetic fields is still under development (see e.g. Potter et al. 2012, for a different rotation-magnetic field interaction theory, the $\alpha - \Omega$ dynamo, and its impact on massive star evolution) and the next 10 years will certainly provide new insights on this important topic.

Other Input Physics

The other key input physics that are essentials for the computation of stellar evolution models are: nuclear reactions, mass loss prescriptions (discussed above),

the equation of state, opacities and neutrino losses. Stellar evolution codes are now able to include larger and more flexible nuclear reaction network (see e.g. Frischknecht et al. 2010, for a description of the implementation of a flexible network in GENEC). Nuclear physics and other inputs are described for other codes for example in Paxton et al. (2011) and Chieffi et al. (1998).

In this chapter, the evolution of single stars is discussed. We refer the reader to Langer (2012) for a review of the impact of binarity on massive star evolution and to Schneider et al. (2014) for the possible impact of a binary companion on the properties of VMS. Note that the mass transfer efficiency prescriptions used in binary model represent an important uncertainty, especially for VMS with high luminosities.

6.3 General Properties and Early Evolution of VMS

6.3.1 VMS Evolve Nearly Homogeneously

Probably the main characteristic that makes VMS quite different from their lower mass siblings is the fact that they possess very large convective cores during the MS phase. They therefore evolve quasi-chemically homogeneously even if there is no mixing (due e.g. by rotation) in radiative zones as discussed in Maeder (1980). To illustrate this last point, Fig. 6.3 shows the convective core mass fraction for

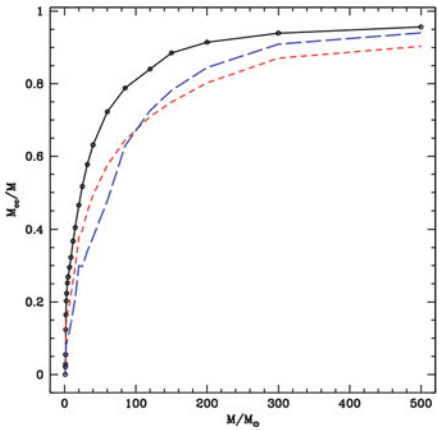

Fig. 6.3 Mass fraction of the convective core in non-rotating solar metallicity models. This figure and all the following figures are taken from Yusof et al. (2013). Models with initial masses superior or equal to 150 M are from Yusof et al. (2013). Models for lower initial masses are from Ekström et al. (2012). The *continuous line* corresponds to the ZAMS, the *short-dashed line* to models when the mass fraction of hydrogen at the centre, X_c, is 0.35, and the *long-dashed line* to models when X_c is equal to 0.05

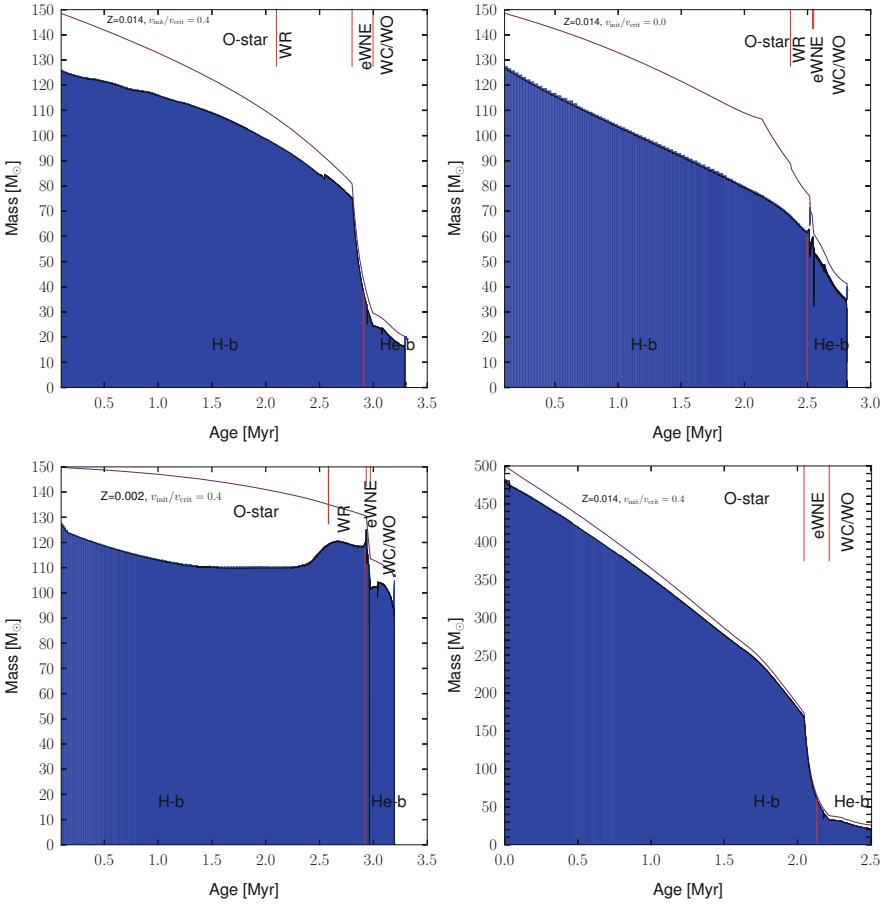

Fig. 6.4 Structure evolution as a function of age for selected models: solar metallicity 150 $M_\odot$ rotating (*top-left*) and non-rotating (*top-right*) models, rotating SMC metallicity 150 $M_\odot$ model (*bottom-left*) and rotating solar metallicity 500 $M_\odot$ model (*bottom-right*). The *blue zones* represent the convective regions. The *top solid black line* indicates the total mass of the star and *vertical red markers* are given for the different phases (O-type, WR = eWNL, eWNE and WC/WO) at the top of the plots. The transition between H- and He-burning phases is indicated by the *red vertical line* at the *bottom* of the plots

non-rotating massive stars at solar metallicity. It is apparent that the convective cores for masses above 150 $M_\odot$ extend over more than 75 % of the total mass of the star.

Figure 6.4 shows how age, metallicity and rotation influence this mass fraction. Comparing the *top-left* and *bottom-left* panels showing the rotating 150 $M_\odot$ models at solar and SMC metallicities (Z), respectively, we can see that the convective core occupies a very slightly larger fraction of the total mass at SMC metallicity on the ZAMS. As for lower-mass massive stars, this is due to a lower CNO content leading to higher central temperature. This effect is counterbalanced by the lower

opacity (especially at very low metallicities) and the net change in convective core size is small. As the evolution proceeds mass loss is weaker at lower Z and thus the total mass decreases slower than the convective core mass. This generally leads to a smaller fraction of the total mass occupied by the convective core in the SMC models.

We can see the impact of rotation by comparing the rotating (*top-left*) and non-rotating (*top-right*) 150 $M_\odot$ models. The convective core size remains higher in the rotating model due to the additional mixing in radiative zones. We can see that rotation induced mixing can even lead to an increase of the convective core size as is the case for the SMC model (*bottom-left*). This increase is typical of quasi-chemically homogeneous evolution also found in previous studies (see Yoon et al. 2012, and citations therein). The rotating 500 $M_\odot$ model (*bottom-right* panel) evolves quasi-homogeneously throughout its entire evolution, even with an initial ratio of the velocity to the critical velocity of 0.4.

These features, very large convective cores and quasi-chemi homogeneous evolution, are key factors governing their evolution as is discussed below.

6.3.2 Evolutionary Tracks

In Figs. 6.5 and 6.6, we present the evolutionary tracks of models with initial masses between 150 and 500 $M_\odot$ at various metallicities. Other properties of VMS models at the end of H- and He- burning stages are given in Tables 6.1 and 6.2, respectively.

A very first striking feature is that these massive stars evolve vertically in the HR diagram (HRD) covering only very restricted ranges in effective temperatures but a very large range in luminosities. This is typical of an evolution mainly governed by mass loss and also by a strong internal mixing (here due to convection).

Let us now describe in more details the evolution of the non-rotating 500 $M_\odot$ model at solar metallicity (see Fig. 6.5). In general, the luminosity of stars increases during the MS phase. Here we have that during that phase, the luminosity decreases slightly by about 0.1 dex. This is the consequence of very high mass loss rates (of the order of 7×10^{-5} $M_\odot$ per year) already at very early evolutionary stages.

At an age of 1.43 million years, the mass fraction of hydrogen at the surface becomes inferior to 0.3, the star enters into the WR phase and has an actual mass decreased by about 40 % with respect to its initial value. At that time the mass fraction of hydrogen in the core is 0.24. Thus this star enters the WR phase while still burning hydrogen in its core and having nearly the same amount of hydrogen at the centre and at the surface, illustrating the nearly homogeneous nature of its evolution (see also Maeder 1980). Typically for this model, the convective core encompasses nearly 96 % of the total mass on the ZAMS (see also Fig. 6.3).

At an age equal to 2.00 Myr, the mass fraction of hydrogen is zero in the core ($X_c = 0$). The star has lost a huge amount of mass through stellar winds and has at this stage an actual mass of 55.7 $M_\odot$. So, since the entrance into the WR phase, the

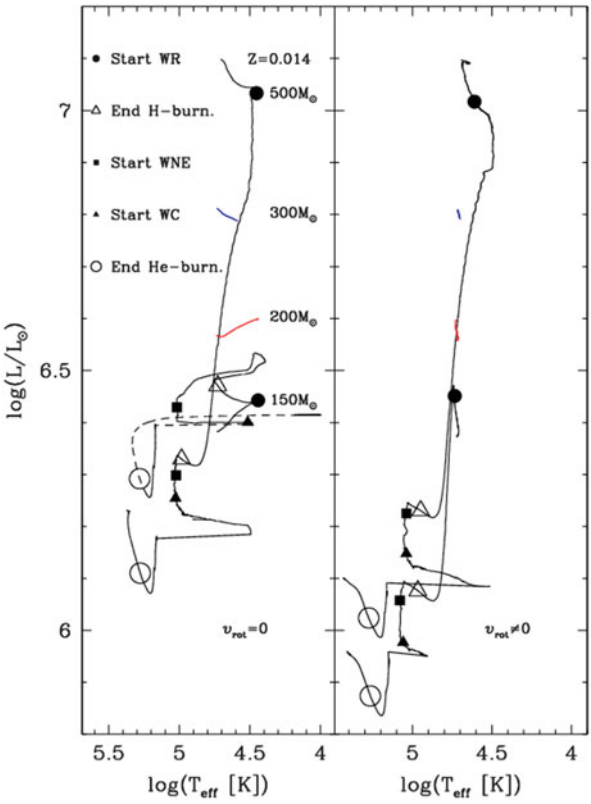

Fig. 6.5 HR diagram from 150 up to 500 $M_\odot$ at solar metallicity for non-rotating (*left*) and rotating (*right*) models, respectively. Key stages are indicated along the tracks. Only the first portion (up to start of WR phase) of the tracks for the 200 and 300 $M_\odot$ are shown

star has lost about 245 $M_\odot$, i.e. about half of its total mass. This strong mass loss episode translates into the HR diagram by a very important decrease in luminosity. Note that when X_c is zero, the convective core still encompass 80 % of the total stellar mass!

The core helium burning phase last for about 0.3 Myr, that means slightly more than 15 % of the MS lifetime. At the end of the core He burning phase, the actual mass of the star is 29.82 $M_\odot$, its age is 2.32 My, the mass fraction of helium at the surface is 0.26. The total WR phase lasts for 0.88 My, that means about 38 % of the total stellar lifetime.

It is interesting to compare the evolution of the 500 $M_\odot$ stellar model with that of the 150 $M_\odot$ model. In contrast to the 500 $M_\odot$ model, the 150 $M_\odot$ increases in luminosity during the MS phase. Looking at the HRD we see that the O-type star phases of the 150 and 500 $M_\odot$ models cover more or less the same effective temperature range. This illustrates the well known fact that the colors of stars for this mass range does not change much with the initial mass.

When the stars enters into the WR phase, in contrast to the case of the 500 $M_\odot$ where the luminosity decreases steeply, the luminosity of the 150 $M_\odot$ model continues to increase a little. The luminosities of the two models when the hydrogen

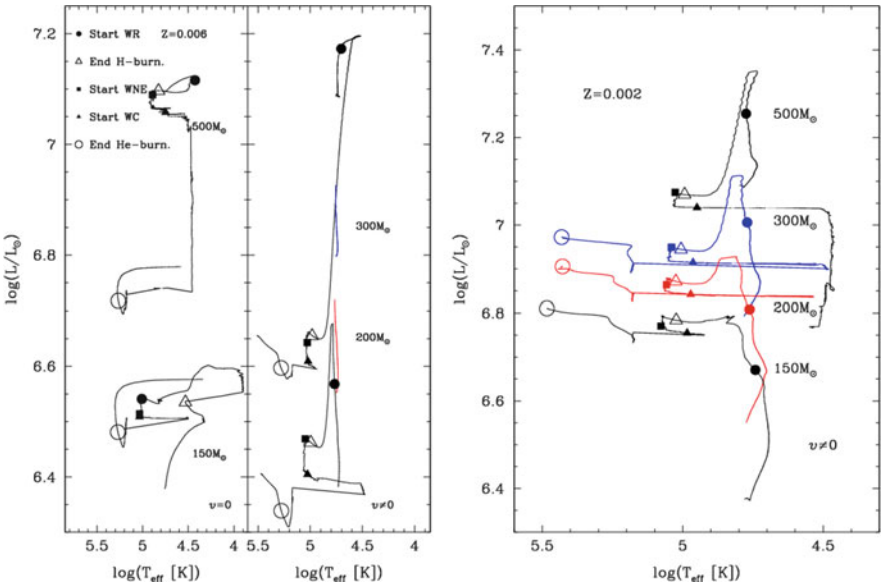

Fig. 6.6 Same as Fig. 6.5 for *right*: LMC models ($Z = 0.006$) and *right*: SMC rotating models ($Z = 0.002$)

mass fraction at the surface becomes inferior to 10^{-5} differ by just a little more than 0.1 dex. The effective temperatures are similar. Thus one expects stars from very different initial masses to occupy similar positions in the HRD (the 500 $M_\odot$ star being slightly less luminous than the 150 $M_\odot$ during the WR phase). We note that after the end of the core He-burning phase, the star evolves to the red and terminate its lifetime around an effective temperature of Log $T_{\rm eff}$ equal to 4. This comes from the core contraction at the end of core He-burning which releases energy and leads to an envelope expansion akin to the expansion of the envelope at the end of the MS (see also Yoshida and Umeda 2011).

The duration of the core H-burning phase of the 150 $M_\odot$ model is not much different from the one of the 500 $M_\odot$ model being 2.5 My instead of 2 My. The core He-burning lifetime lasts for 0.3 My as for the 500 $M_\odot$. The total duration of the WR phase is 0.45 My, thus about half of the WR duration for the 500 $M_\odot$.

The 200 $M_\odot$ model has an evolution similar to the 150 $M_\odot$ model, while the 300 $M_\odot$ has an evolution similar to the 500 $M_\odot$.

Let us now consider how rotation changes the picture. The right panel of Fig. 6.5 shows the evolutionary tracks of the $Z = 0.014$ rotating models in a similar way to the tracks of the non-rotating models in the left panel. The changes brought by rotation are modest. This is expected because of two facts: first, in this high mass range, the evolution is more impacted by mass loss than by rotation, second, stars are already well mixed by the large convective cores. One notes however a few differences between the non-rotating and rotating models. One of the most

Table 6.1 Properties of the hydrogen burning phase: initial properties of stellar models (columns 1–3), lifetime of H-burning and O-type star phase (4–5), average MS surface velocity (6) and properties at the end of the core H-burning phase (7–15). Masses are in solar masses, velocities are in $\mathrm{km\,s^{-1}}$, lifetimes are in 10^6 years and abundances are surface abundances in mass fractions. The luminosity, L, is in $\log_{10}(L/L_\odot)$ unit and the effective temperature, T_{eff}, is in $\log_{10}$ [K]. Note that the effective temperature given here includes a correction for WR stars to take into account the fact that their winds are optically thick as in Meynet and Maeder (2005)

M_{ini}	Z_{ini}	$\frac{v_{\mathrm{ini}}}{v_{\mathrm{crit}}}$	τ_H	τ_o	$\langle v_{\mathrm{MS}}\rangle$	$M^{\mathrm{end}}_{\mathrm{H.b.}}$	^{1}H	^{4}He	^{12}C	^{14}N	^{16}O	T_{eff}	L	Γ_{Edd}
120	0.014	0.0	2.671	2.592	0.0	63.7	2.04e-1	7.82e-1	8.58e-5	8.15e-3	1.06e-4	4.405	6.334	0.627
150	0.014	0.0	2.497	2.348	0.0	76.3	1.35e-1	8.51e-1	9.26e-5	8.15e-3	9.91e-5	4.413	6.455	0.657
200	0.014	0.0	2.323	2.095	0.0	95.2	7.51e-2	9.11e-1	9.93e-5	8.14e-3	9.23e-5	4.405	6.597	0.687
300	0.014	0.0	2.154	1.657	0.0	65.2	1.24e-3	9.85e-1	1.31e-4	8.11e-3	7.93e-5	4.267	6.401	0.595
500	0.014	0.0	1.990	1.421	0.0	56.3	2.20e-3	9.84e-1	1.26e-4	8.12e-3	8.03e-5	4.301	6.318	0.568
120	0.014	0.4	3.137	2.270	116.71	34.6	1.56e-3	9.85e-1	1.33e-4	8.10e-3	8.48e-5	4.400	6.018	0.463
150	0.014	0.4	2.909	2.074	101.24	37.1	1.80e-3	9.85e-1	1.30e-4	8.11e-3	8.41e-5	4.387	6.062	0.479
200	0.014	0.4	2.649	1.830	89.33	40.0	1.41e-3	9.85e-1	1.33e-4	8.10e-3	8.30e-5	4.372	6.110	0.495
300	0.014	0.4	2.376	1.561	61.16	43.2	1.85e-3	9.85e-1	1.33e-4	8.10e-3	8.23e-5	4.356	6.157	0.511
500	0.014	0.4	2.132	1.377	24.55	48.1	1.24e-3	9.85e-1	1.38e-4	8.10e-3	8.08e-5	4.332	6.221	0.531
120	0.006	0.0	2.675	2.682	0.0	79.0	4.03e-1	5.91e-1	3.29e-5	3.50e-3	4.47e-5	4.441	6.391	0.672
150	0.006	0.0	2.492	2.499	0.0	96.1	3.28e-1	6.67e-1	3.58e-5	3.50e-3	4.25e-5	4.483	6.524	0.709
500	0.006	0.0	1.904	1.636	0.0	238.8	2.56e-2	9.69e-1	5.12e-5	3.48e-3	3.18e-5	4.032	7.094	0.819
120	0.006	0.4	3.140	2.479	208.55	64.0	1.70e-3	9.92e-1	6.06e-5	3.47e-3	3.04e-5	4.387	6.395	0.597
150	0.006	0.4	2.857	2.172	198.19	71.3	9.76e-4	9.93e-1	6.33e-5	3.47e-3	2.97e-5	4.365	6.455	0.615
200	0.006	0.4	2.590	1.894	193.05	80.7	1.22e-3	9.93e-1	6.29e-5	3.47e-3	2.95e-5	4.339	6.525	0.638
300	0.006	0.4	2.318	1.619	173.47	85.8	1.32e-3	9.93e-1	6.30e-5	3.47e-3	2.93e-5	4.327	6.559	0.649
500	0.006	0.4	2.077	1.419	116.76	101.7	1.37e-3	9.93e-1	6.37e-5	3.47e-3	2.89e-5	4.291	6.650	0.676
150	0.002	0.4	2.921	2.567	318.92	128.8	1.67e-3	9.96e-1	2.13e-5	1.16e-3	8.09e-6	4.394	6.780	0.720
200	0.002	0.4	2.612	2.168	333.43	152.2	1.31e-3	9.97e-1	2.26e-5	1.16e-3	7.82e-6	4.363	6.867	0.743
300	0.002	0.4	2.315	1.801	347.32	176.2	1.10e-3	9.97e-1	2.32e-5	1.16e-3	7.68e-6	4.279	7.067	0.763

Table 6.2 Properties of the helium burning phase: initial properties of stellar models (columns 1–3), age of star at the end of He-burning (4), average He-b. surface velocity (5) and properties at the end of the core He-burning phase (6–15). Abundances are given for the surface, except for $^{12}C_c$, which represents the central C abundance. Same units as in Table 6.1. $\mathcal{L}_{CO}$ [10^{50} $\frac{g\,cm^2}{s}$] is the angular momentum contained in the CO core (Note that at this stage the angular velocity is constant in the CO core due to convective mixing)

M_{ini}	Z_{ini}	$\frac{v_{ini}}{v_{crit}}$	$age^{end}_{He-b.}$	$\langle v_{He-b.}\rangle$	$M^{end}_{He-b.}$	^{4}He	^{12}C	$^{12}C_c$	^{16}O	^{22}Ne	T_{eff}	L	Γ_{Edd}	$\mathcal{L}_{CO}$
120	0.014	0.0	3.003	0.00	30.9	0.242	0.458	0.150	0.281	1.081e-02	4.819	6.117	0.650	0
150	0.014	0.0	2.809	0.00	41.3	0.234	0.436	0.126	0.312	1.003e-02	4.822	6.278	0.706	0
200	0.014	0.0	2.622	0.00	49.4	0.207	0.408	0.112	0.366	8.811e-03	4.807	6.377	0.737	0
300	0.014	0.0	2.469	0.00	38.2	0.234	0.443	0.133	0.305	1.029e-02	4.825	6.236	0.691	0
500	0.014	0.0	2.314	0.00	29.8	0.261	0.464	0.152	0.257	1.110e-02	4.811	6.095	0.640	0
120	0.014	0.4	3.513	1.58	18.8	0.292	0.492	0.195	0.198	1.196e-02	4.806	5.814	0.533	1.91
150	0.014	0.4	3.291	1.18	20.3	0.286	0.488	0.187	0.208	1.184e-02	4.808	5.863	0.551	1.91
200	0.014	0.4	3.020	0.50	22.0	0.277	0.484	0.180	0.221	1.172e-02	4.812	5.912	0.570	1.37
300	0.014	0.4	2.733	0.13	24.0	0.270	0.479	0.172	0.233	1.151e-02	4.814	5.965	0.589	0.75
500	0.014	0.4	2.502	0.03	25.9	0.269	0.473	0.164	0.239	1.140e-02	4.811	6.010	0.606	0.28
120	0.006	0.0	2.993	0.00	54.2	0.229	0.391	0.098	0.372	3.701e-03	4.860	6.424	0.753	0
150	0.006	0.0	2.845	0.00	59.7	0.241	0.370	0.086	0.380	3.597e-03	4.844	6.474	0.767	0
500	0.006	0.0	2.182	0.00	94.7	0.251	0.392	0.078	0.349	3.318e-03	4.833	6.711	0.834	0
120	0.006	0.4	3.472	6.84	39.3	0.294	0.457	0.132	0.241	4.709e-03	4.387	6.395	0.692	16.2
150	0.006	0.4	3.164	3.67	45.7	0.310	0.451	0.122	0.231	4.701e-03	4.824	6.329	0.767	14.7
200	0.006	0.4	2.904	1.33	51.1	0.303	0.444	0.114	0.245	4.547e-03	4.825	6.390	0.738	9.98
300	0.006	0.4	2.625	0.35	54.1	0.291	0.439	0.110	0.262	4.433e-03	4.830	6.421	0.748	5.18
500	0.006	0.4	2.387	0.13	74.9	0.330	0.425	0.090	0.237	4.356e-03	4.790	6.590	0.798	4.83
150	0.002	0.4	3.193	64.94	106.7	0.809	0.153	0.074	0.035	1.730e-03	4.743	6.766	0.841	412.5
200	0.002	0.4	2.889	29.88	129.3	0.880	0.109	0.066	0.009	1.777e-03	4.789	6.861	0.863	355.6
300	0.002	0.4	2.585	5.10	149.8	0.938	0.058	0.060	0.001	1.798e-03	4.833	6.933	0.880	156.8

striking differences is the fact that the models during their O-type phase evolve nearly vertically when rotation is accounted for. This is the effect of rotational mixing which keeps the star more chemically homogeneous than in the non-rotating cases (although, as underlined above, already in models with no rotation, due to the importance of the convective core, stars are never very far from chemical homogeneity). As was the case in the non-rotating tracks, the O-type star phase corresponds to an upward displacement when time goes on in the HR diagram for the 150 $M_\odot$ model, while, it corresponds to a downwards displacement for the three more massive models. One notes finally that lower luminosities are reached by the rotating models at the end of their evolution (decrease by about 0.3 dex in luminosity, thus by a factor 2). This comes mainly because the rotating models enter earlier into their WR phase and thus lose more mass.

How does a change in metallicity alter the picture? When the metallicity decreases to Z = 0.006 (see Fig. 6.6, *left*), as expected, tracks are shifted to higher luminosities and effective temperatures. In this metallicity range, all models evolve upwards during their O-type star phase in the HR diagram. This is an effect of the lower mass loss rates.

As was already the case at Z = 0.014, rotation makes the star evolve nearly vertically in the HR diagram. One notes in this metallicity range, much more important effects of rotation than at Z = 0.014, which is also expected, since at these lower metallicity, mass loss rates are smaller and rotational mixing more efficient. We note that most of the decrease in luminosity in the 500 $M_\odot$ solar mass model occurs during the WC phase in the Z = 0.006 non-rotating model, while it occurs during the WNL phase in the rotating one. This illustrates the fact that rotational mixing, by creating a much larger H-rich region in the star, tends to considerably increase the duration of the WNL phase. One notes also that while the 150 $M_\odot$ model enters the WR phase only after the MS phase, the rotating model becomes a WR star before the end of the MS phase.

At the metallicity of the SMC (see Fig. 6.6, *right*), except for the 500 $M_\odot$, the tracks evolve horizontally after the end of the core H-burning phase (triangle in Fig. 6.6, *right*). The much lower mass loss rates are responsible for this effect.

6.3.3 *Lifetimes and Mass-Luminosity Relation*

In Tables 6.1 and 6.2, we provide ages at the end of core hydrogen burning and core helium burning, respectively. We see that the MS lifetime of non-rotating models at solar metallicity ranges from 2.67 to 1.99 Myr for initial masses ranging from 120 to 500 $M_\odot$ showing the well known fact that VMS have a very weak lifetime dependence on their initial mass.

The mass-luminosity relation on the ZAMS for rotating massive stars at solar composition is shown in Fig. 6.7. The relation ($L \propto M^\alpha$) is steep for low and intermediate-mass stars ($\alpha \sim 3$ for $10 < M/M_\odot < 20$) and flattens for VMS ($\alpha \sim 1.3$ for $200 < M/M_\odot < 500$). This flattening is due to the increased radiation

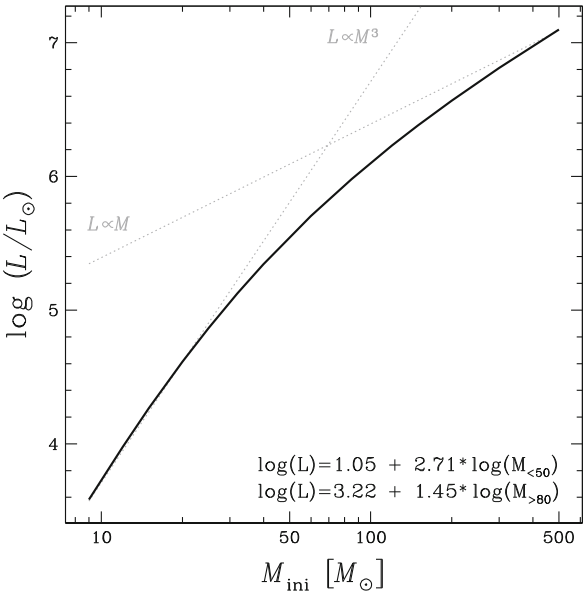

Fig. 6.7 Mass-luminosity relation on the ZAMS for rotating models at solar metallicity. The formulae in the bottom right corner are linear fits for the mass ranges: 9–50 $M_\odot$ and 80–500 $M_\odot$. The non-rotating models have very similar properties on the ZAMS

pressure relative to gas pressure in massive stars. Since the lifetime of a star is roughly M/L, we get that for VMS $\tau \propto M/L \propto M^{-0.3}$.

The H-burning (and total) lifetimes of VMS are lengthened by rotation as in lower mass stars. Differences in the H-burning lifetimes of rotating and non-rotating 150 $M_\odot$ models at solar metallicity are $\sim$14 %. The effects of metallicity on the lifetimes are generally very small. The small differences in total lifetimes are due to different mass loss at different metallicities.

6.3.4 Mass Loss by Stellar Winds

Mass loss by stellar winds is a key factor governing the evolution of VMS. This comes from the very high luminosities reached by these objects. For example, the luminosity derived for R136a1 is about 10 million times that of our sun.

For such luminous objects, winds will be very powerful at all evolutionary stages, so while early main-sequence VMS are formally O-type stars from an evolutionary perspective, their spectral appearance may be closer to Of or Of/WN at early phases (Crowther et al. 2012).

Table 6.3 gives the total mass at the start and end of the evolution[2] as well as at the transitions between the different WR phases in columns 1 to 5. The average

[2]The models have been evolved beyond the end of core He-burning and usually until oxygen burning, thus very close to the end of their life (see Yusof et al. 2013, for full details)

Table 6.3 Mass loss properties: Total mass of the models at various stages (columns 1–5), and average mass loss rates $\langle \dot{M} \rangle$ during the O-type and eWNE phases (6,7). Masses are in solar mass units and mass loss rates are given in $M_\odot$ year^{-1}

ZAMS	start eWNL	start eWNE	start WC	final	$\langle \dot{M}_{\rm Vink} \rangle$	$\langle \dot{M}_{\rm eWNE} \rangle$
	Z = 0.014, $v/v_{crit} = 0.0$					
120	69.43	52.59	47.62	30.81	2.477e-05	3.638e-04
150	88.86	66.87	61.20	41.16	3.274e-05	6.107e-04
200	121.06	91.20	83.85	49.32	4.618e-05	1.150e-03
300	184.27	130.47	52.05	38.15	8.047e-05	8.912e-04
500	298.79	169.50	45.14	29.75	1.736e-04	9.590e-04
	Z = 0.014, $v/v_{crit} = 0.4$					
120	88.28	69.54	27.43	18.68	1.675e-05	2.057e-04
150	106.64	80.88	29.49	20.22	2.467e-05	2.640e-04
200	137.52	98.75	31.84	21.93	3.985e-05	3.564e-04
300	196.64	129.10	34.45	23.93	7.559e-05	5.160e-04
500	298.42	174.05	38.30	25.83	1.594e-04	7.901e-04
	Z = 0.006, $v/v_{crit} = 0.0$					
120	74.30	57.91	56.91	54.11	2.140e-05	3.272e-04
150	94.18	74.20	71.75	59.59	2.839e-05	5.038e-04
500	332.68	250.64	197.41	94.56	1.304e-04	3.334e-03
	Z = 0.006, $v/v_{crit} = 0.4$					
120	100.57	90.78	54.43	39.25	9.429e-06	3.219e-04
150	125.79	111.84	60.75	45.58	1.367e-05	4.418e-04
200	166.81	144.86	66.25	51.02	2.180e-05	6.257e-04
300	247.07	207.10	73.11	54.04	4.166e-05	9.524e-04
500	397.34	315.51	86.10	74.75	9.194e-05	1.685e-03
	Z = 0.002, $v/v_{crit} = 0.4$					
150	135.06	130.46	113.51	106.50	6.661e-06	4.485e-04
200	181.42	174.18	137.90	129.21	9.902e-06	6.631e-04
300	273.18	260.81	156.14	149.70	1.730e-05	1.040e-03

mass loss rates during the O-type and eWNE phases (the phase during which the mass loss rates are highest) are given in columns 6 and 7, respectively.

The evolution of the mass loss rates for various models are shown in Fig. 6.8. Following the evolution from left to right for the 150 $M_\odot$ model at solar metallicity (solid-black), mass loss rates slowly increase at the start of the O-type phase with mass loss rates between 10^{-5} $M_\odot$ year^{-1} (absolute values for the mass loss rates, $-\dot{M}$, are quoted in this paragraph) and $10^{-4.5}$ $M_\odot$ year^{-1}. If a bi-stability limit is encountered during the MS phase, as is the case in the non-rotating 150 $M_\odot$ model, mass loss rates can vary significantly over a short period of time and mass loss peaks reach values higher than 10^{-4} $M_\odot$ year^{-1}. The highest mass loss rate is encountered at the start of the eWNE phase (star symbols) with values in excess of 10^{-3} $M_\odot$ year^{-1} (note that the mass loss rate in the non-rotating model has a peak at the end of the H-burning phase. phase due to the star reaching temporarily

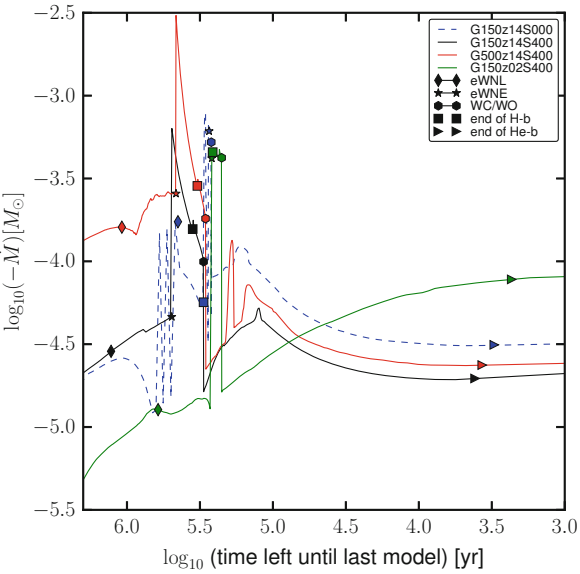

Fig. 6.8 Evolution of the mass loss rate as a function of time left until last model (log scale) for the rotating 500 $M_\odot$ model (*solid-red*), the rotating 150 $M_\odot$ model (*solid-black*), the non-rotating (*dashed*) 150 $M_\odot$ model at solar metallicity, and the rotating 150 $M_\odot$ model at SMC metallicity (*solid-green*). The diamonds indicate the start of the eWNL phase, the stars the start of the eWNE phase and hexagons the start of the WC/WO phase. The *squares* and *triangles* indicate the end of H-b. and He-b. phases, respectively

cooler effective temperatures). Such high mass loss rates quickly reduce the mass and luminosity of the star and thus the mass loss rate also decreases quickly during the eWNE phase. During the WC/WO phase, mass loss rates are of the same order of magnitude as during the O-type phase.

Comparing the rotating 500 and 150 $M_\odot$ model at solar metallicity (solid black and red), we see that more massive stars start with higher mass loss rates but converge later on to similar mass loss rates since the total mass of the models converges to similar values (see Table 6.3).

Comparing the SMC and solar metallicity 150 $M_\odot$ rotating models, we can clearly see the metallicity effect during the O-type star phase. During the eWNE phase, mass loss rates are similar and in the WC/WO, mass loss rates in the SMC model are actually higher since the total mass in that model remained high in contrast with solar metallicity models.

Table 6.3 also shows the relative importance of the mass lost during the various phases and how their importance changes as a function of metallicity. Even though mass loss is the strongest during the eWNE phase, significant amount of mass is lost in all phases.

6.3.5 *Mass Loss Rates and Proximity of the Eddington Limit*

Vink et al. (2011b) suggest enhanced mass-loss rates (with respect to Vink et al. 2001a, used in the models presented here) for stars with high Eddington parameters (($\Gamma_e \geq 0.7$), see Eq. 1 in Vink et al. 2011b, for the exact definition of Γ_e) that they

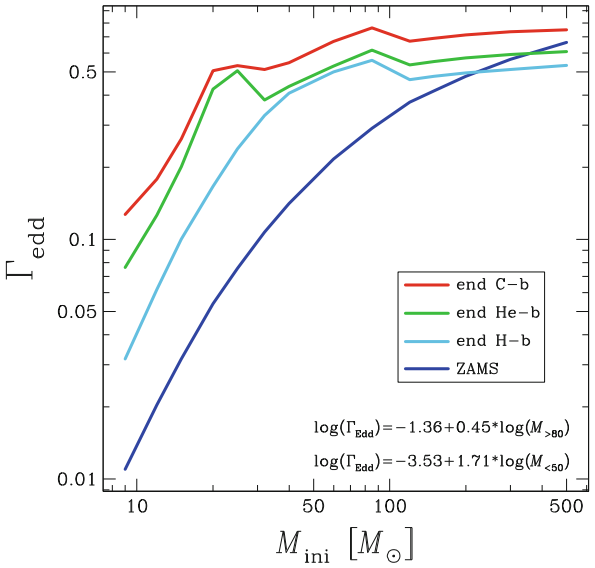

Fig. 6.9 Eddington parameter, $\Gamma_{\rm edd}$ for rotating models at solar metallicity. $\Gamma_{\rm edd}$ is plotted on the ZAMS (*blue line*) and the end of H-(*light blue*), He-(*green*) and C-burning (*red*) phases. Except for the 300 and 500 $M_\odot$ models, $\Gamma_{\rm edd}$ increases throughout the evolution. At solar metallicity, the highest value (close to 0.8) is actually reached by the 85 $M_\odot$ model at the end of its evolution. This could lead to significant mass loss shortly before the final explosion in a model that ends as a WR star and potentially explain supernova surrounded by a thick circumstellar material without the need for the star to be in the luminous variable phase. The formulae in the bottom right corner are linear fits for the mass ranges: 9–50 $M_\odot$ and 80–500 $M_\odot$. The non-rotating models have very similar properties on the ZAMS

attribute to the Wolf-Rayet stage. In order to know whether higher mass loss rates near the Eddington limit could have an impact on the present result, we discuss here the proximity of our models to the Eddington limit.

Figure 6.9 shows the Eddington parameter, $\Gamma_{\rm Edd} = L/L_{\rm Edd} = \kappa L/(4\pi cGM)$, as a function of the initial mass of our models at key stages. Since the Eddington parameter, $\Gamma_{\rm Edd}$ scales with L/M, the curve for $\Gamma_{\rm Edd}$ also flattens for VMS. The ZAMS values for $\Gamma_{\rm Edd}$ range between 0.4 and 0.6, so well below the Eddington limit, $\Gamma_{\rm Edd} = 1$, and below the limiting value of $\Gamma_{\rm e} = 0.7$ where enhanced mass-loss rates are expected according to Vink et al. (2011b).

How does $\Gamma_{\rm Edd}$ change during the lifetime of VMS? Figure 6.10 presents the evolution of $\Gamma_{\rm Edd}$ for a subset of representative models. The numerical values for each model are given at key stages in Tables 6.1 and 6.2. Since $\Gamma_{\rm Edd} \propto \kappa L/M$, an increase in luminosity and a decrease in mass both lead to higher $\Gamma_{\rm Edd}$. Changes in effective temperature and chemical composition affect the opacity and also lead to changes in $\Gamma_{\rm Edd}$.

In rotating models at solar metallicity, $\Gamma_{\rm Edd}$ slowly increases until the start of the eWNE phase. This is mainly due to the increase in luminosity and decrease in mass

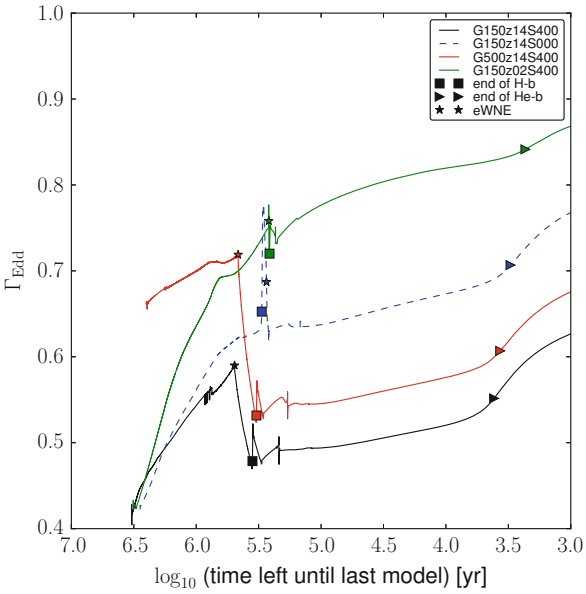

Fig. 6.10 Evolution of the Eddington parameter, $\Gamma_{\rm Edd}$, as a function of time left until last model (log scale) for the rotating 500 $M_\odot$ model (*solid-red*), the rotating 150 $M_\odot$ model (*solid-black*), the non-rotating (*dashed*) 150 $M_\odot$ model at solar metallicity, and the rotating 150 $M_\odot$ model at SMC metallicity (*solid-green*). The stars indicate the start of the eWNE phase. The squares and triangles indicate the end of H-b. and He-b. phases, respectively

of the model. At the start of the eWNE phase, mass loss increases significantly. This leads to a strong decrease in the luminosity of the model and as a result $\Gamma_{\rm Edd}$ decreases sharply.

During the WC/WO phase, mass loss rates being of similar values as during the O-type star phase, $\Gamma_{\rm Edd}$ increases again gradually.

We can see that, at solar metallicity, $\Gamma_{\rm Edd}$ rarely increases beyond 0.7 even in the 500 $M_\odot$ model. There are nevertheless two interesting cases in which values above 0.7 are reached. The first case is during the advanced stages. At this stage, mass loss does not have much time to change the total mass of the star (it is mostly changes in effective temperature and to a minor extent in luminosity that influence the increase in $\Gamma_{\rm Edd}$). This may nevertheless trigger instabilities resulting in strong mass loss episodes. This may have consequences for the type of SN event that such a star will produce and may be a reason why the explosion of VMS may look like as if they had happened in an environment similar to those observed around Luminous Blue Variable. The second case is at low metallicity, as highlighted by the 150 $M_\odot$ model at SMC metallicity. Indeed, values above 0.7 are reached before the end of the MS (square symbol). Mass loss prescriptions such as the ones of Vink et al. (2011b) and Maeder et al. (2012) may thus play an important role on the fate of VMS. The non-rotating model has a different mass loss history (see Fig. 6.8), which explains the slightly different evolution of $\Gamma_{\rm Edd}$ near the end of the main sequence.

6.3.6 *Evolution of the Surface Velocity*

The surface velocity of stars is affected by several processes. Contraction or expansion of the surface respectively increases and decreases the surface velocity due to the conservation of angular momentum. Mass loss removes angular momentum and thus decreases the surface velocity. Finally internal transport of angular momentum generally increases the surface velocity. As shown in Fig. 6.11 (left panel), at solar metallicity, the surface velocity rapidly decreases during the main sequence due to the strong mass loss over the entire mass range of VMS. At SMC metallicity, mass loss is weaker than at solar metallicity and internal transport of angular momentum initially dominates over mass loss and the surface velocity increases during the first half of the MS phase. During this time, the ratio of surface velocity to critical velocity also increases up to values close to 0.7 (note that the models presented include the effect of the luminosity of the star when determining the critical rotation as described in Maeder and Meynet 2000). However, as the evolution proceeds, the luminosity increases and mass loss eventually starts to dominate and the surface velocity and its ratio to critical rotation both decrease for the rest of the evolution. SMC stars thus never reach critical rotation. The situation at very low and zero metallicities has been studied by several groups (see Hirschi 2007; Ekström et al. 2008; Yoon et al. 2012; Chatzopoulos and Wheeler 2012, and references therein). If mass loss becomes negligible, then the surface velocity reaches critical rotation for a large fraction of its lifetime, which probably leads to mechanical mass loss along the equator. The angular momentum content in the core of VMS stars is discussed further in Sect. 6.5.4.

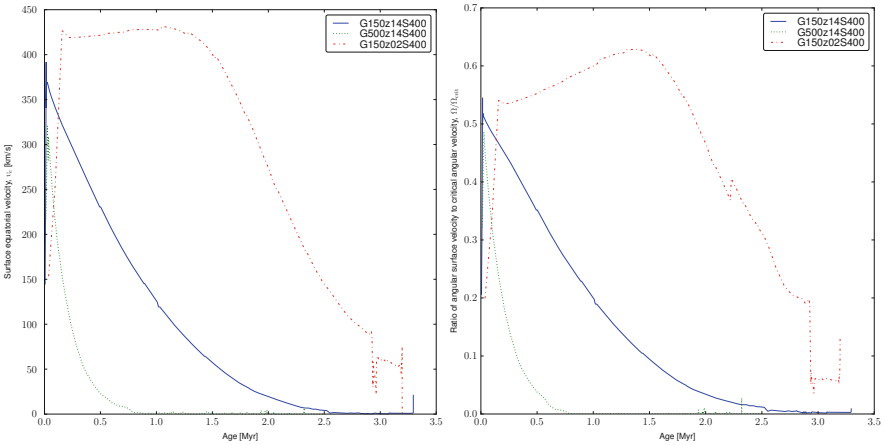

Fig. 6.11 Evolution of surface equatorial velocity (*left*) and ratio of the surface angular velocity to the critical angular velocity (*right*) for the rotating solar metallicity 150 and 500 $M_{\odot}$ and SMC 150 $M_{\odot}$ models as a function of age of the star

6.4 WR Stars from VMS

Figure 6.12 presents the evolution of the surface abundances as a function of the total mass for the solar metallicity rotating models of 150 and 60 $M_{\odot}$. This figure shows how the combined effects of mass loss and internal mixing change their surface composition. Qualitatively there are no big differences between the 60 and 150 $M_{\odot}$ models. Since the 150 $M_{\odot}$ has larger cores, the transition to the various WR stages occurs at larger total masses compared to the 60 $M_{\odot}$ model. It thus confirms the general idea that a more massive (thus more luminous) WR star originates from a more massive O-type star. Figure 6.12 shows that all abundances and abundance ratios are very similar for a given WR phase. It is therefore not easy to distinguish a WR originating from a VMS from its surface chemical composition (however see below).

We present in Table 6.4 the lifetimes of the different WR phases through which all our VMS models evolve. At solar metallicity, the WR phase of non-rotating stellar models for masses between 150 and 500 $M_{\odot}$ covers between 16 and 38 % of the total stellar lifetime. This is a significantly larger proportion than for masses between 20 and 120 $M_{\odot}$, where the WR phase covers only 0–13 % of the total stellar lifetimes. At the LMC metallicity, the proportion of the total stellar lifetime spent

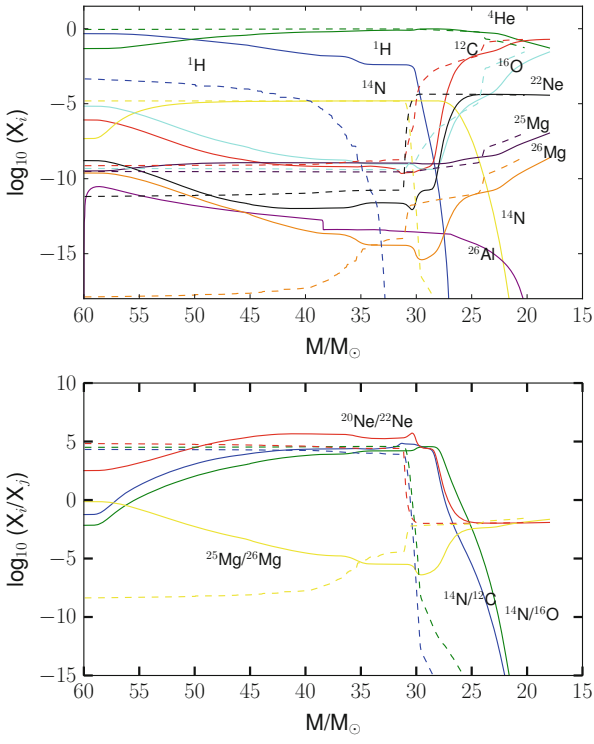

Fig. 6.12 Evolution of surface abundances of the solar metallicity rotating 150 $M_{\odot}$ (*solid*) and 60 $M_{\odot}$ (*dashed*) rotating solar Z models as a function of total mass (evolution goes from left to right since mass loss peels off the star and reduces the total mass). The *top panel* shows individual abundances while the *bottom panel* shows abundance ratios

Table 6.4 Lifetimes of the various phases in units of years

$M_{\rm ini}$	$Z_{\rm ini}$	$\frac{v_{\rm ini}}{v_{\rm crit}}$	O-star	WR	WNL	WNE	WN/WC	WC (WO)
120	0.014	0	2.151e06	3.959e05	1.150e05	9.390e03	2.675e02	2.715e05
150	0.014	0	2.041e06	4.473e05	1.777e05	5.654e03	7.120e02	2.639e05
200	0.014	0	1.968e06	5.148e05	2.503e05	1.773e03	4.576e02	2.626e05
300	0.014	0	1.671e06	8.014e05	5.051e05	9.217e03	2.735e03	2.870e05
500	0.014	0	1.286e06	8.848e05	5.804e05	1.079e04	3.279e03	2.935e05
120	0.014	0.4	2.289e06	1.227e06	8.790e05	4.118e04	4.008e03	3.076e05
150	0.014	0.4	2.105e06	1.189e06	8.567e05	2.579e04	3.649e03	3.068e05
200	0.014	0.4	1.860e06	1.164e06	8.375e05	2.242e04	3.153e03	3.042e05
300	0.014	0.4	1.585e06	1.152e06	8.315e05	1.897e04	2.897e03	3.015e05
500	0.014	0.4	1.422e06	1.083e06	7.663e05	1.830e04	2.899e03	2.990e05
120	0.006	0	2.222e06	2.964e05	2.043e05	1.302e02	6.025e02	9.202e04
150	0.006	0	2.028e06	3.320e05	1.579e05	1.211e03	2.921e02	1.728e05
500	0.006	0	1.388e06	5.362e05	2.690e05	5.211e03	1.350e03	2.620e05
120	0.006	0.4	2.513e06	9.624e05	6.776e05	1.601e04	3.386e03	2.687e05
150	0.006	0.4	2.188e06	9.789e05	6.912e05	2.172e04	2.336e03	2.660e05
200	0.006	0.4	1.922e06	9.848e05	7.073e05	1.347e04	2.757e03	2.640e05
300	0.006	0.4	1.644e06	9.838e05	7.033e05	1.600e04	9.744e02	2.644e05
500	0.006	0.4	1.461e06	9.283e05	6.647e05	9.312e03	6.853e02	2.542e05
150	0.002	0.4	2.583e06	6.119e05	3.691e05	8.459e03	4.874e03	2.343e05
200	0.002	0.4	2.196e06	6.926e05	4.524e05	1.019e04	2.709e03	2.300e05
300	0.002	0.4	1.827e06	7.602e05	5.186e05	1.317e04	1.289e03	2.283e05

as a WR phase for VMS decreases to values between 12 % (150 $M_{\odot}$) and 25 % (500 $M_{\odot}$).

Figure 6.13 shows how these lifetimes vary as a function of mass for non-rotating and rotating solar metallicity models. Looking first at the non-rotating models (Fig. 6.13, *left*), we see that the very massive stars (above 150 $M_{\odot}$) have WR lifetimes between 0.4 and nearly 1 My. The longest WR phase is the WNL phase since these stars spend a large fraction of H-burning in this phase. The duration of the WC phases of VMS is not so much different from those of stars in the mass range between 50 and 120 $M_{\odot}$.

Rotation significantly increases the WR lifetimes. Typically, the WR phase of rotating stellar models for masses between 150 and 500 $M_{\odot}$ covers between 36 and 43 % of the total stellar lifetime. The increase is more important for the lower mass range plotted in the figures. This reflects the fact that for lower initial mass stars, mass loss rates are weaker and thus the mixing induced by rotation has a greater impact. We see that this increase is mostly due to longer durations for the WNL phase, the WC phase duration remaining more or less constant for the whole mass range between 50 and 500 $M_{\odot}$ as was the case for the non rotating models. Rotation has qualitatively similar effects at the LMC metallicities.

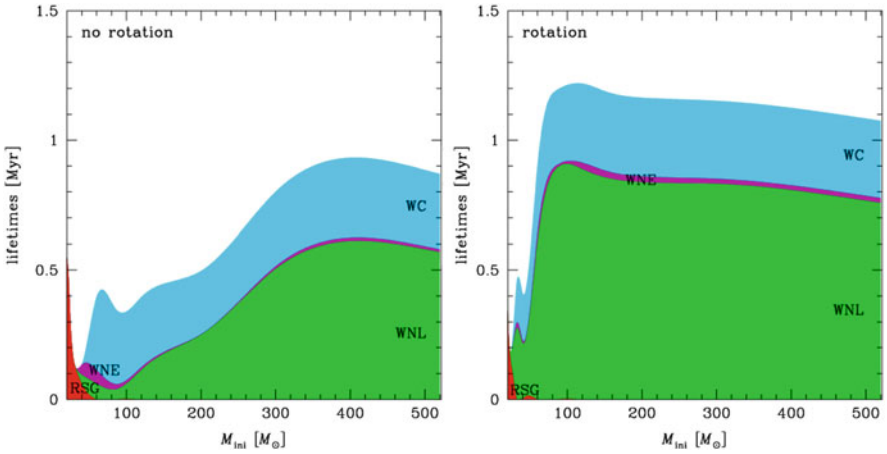

Fig. 6.13 Lifetimes of the RSG phase and of the different WR phases for the solar metallicity non-rotating (*left*) and rotating (*right*) models. Lifetimes are piled up. For example, the lifetime of the WNE phase extent corresponds to the height of the purple area

Would the account of the VMS stars in the computation of the number ratios of WR to O-type stars and on the WN/WC ratios have a significant effect? The inclusion of VMS is marginal at solar metallicity, since the durations are only affected by a factor 2. Convoluted with the weighting of the initial mass function (IMF), WR stars originating from VMS only represent $\sim$ 10 % of the whole population of WR stars (using a Salpeter 1955, IMF) originating from single stars. However, the situation is different at SMC metallicity. Due to the weakness of the stellar winds, single stellar models below 120 $M_\odot$ at this Z do not produce any WC or WO stars (Georgy et al. in prep.). In that case, we expect that the few WC/WO stars observed at low metallicity come from VMS, or from the binary channel (Eldridge et al. 2008). In starburst regions, the detection of WR stars at very young ages would also be an indication that they come from VMS, as these stars enter the WR phase before their less massive counterparts, and well before WRs coming from the binary channel.

We see in Fig. 6.14 that VMS models well fit the most luminous WNL stars. On the other hand, they predict very luminous WC stars. Of course the fact that no such luminous WC stars has ever been observed can simply come from the fact that such stars are very rare and the lifetime in the WC phase is moreover relatively short.

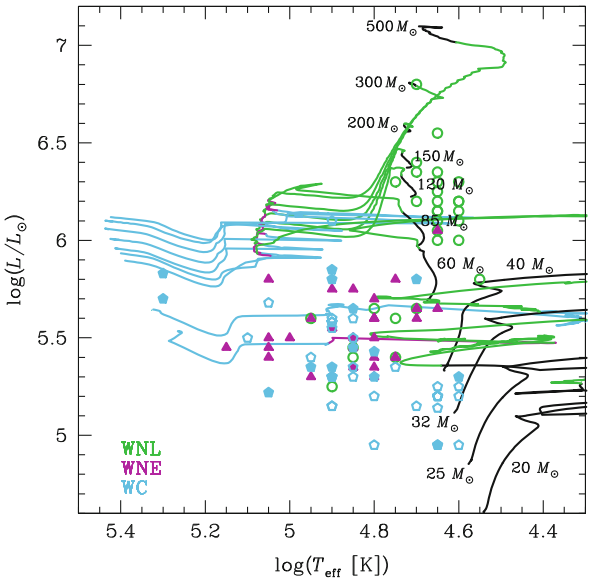

Fig. 6.14 The positions of WR stars observed by Hamann et al. (2006) and Sander et al. (2012) are indicated with the rotating evolutionary tracks taken from Ekström et al. (2012) for masses up to 120 $M_\odot$ and from Yusof et al. (2013) for VMS

6.5 Late Evolution and Pre-SN Properties of Very Massive Stars

The next chapter discusses the explosion that will take place at the end of VMS life but whether or not a star produces a pair-instability supernova (PISN, aka pair-creation SN, PCSN) can be reasonably estimated from the mass of its carbon-oxygen (CO) core as demonstrated by the similar fate for stars with the same CO core found in various studies of VMS in the early Universe (Bond et al. 1984; Heger and Woosley 2002; Chatzopoulos and Wheeler 2012; Dessart et al. 2013), even if their prior evolution is different. In this section, we will thus use the CO core mass to estimate the fate of the models discussed in the previous sections.[3] We will only briefly discuss the supernova types that these VMS may produce in this chapter as this is discussed in Chaps. 7 and 8.

[3]Note that for lower-mass massive stars ($\lesssim$ 50 $M_\odot$), the CO core mass alone is not sufficient to predict the fate of the star and other factors like compactness, rotation and the central carbon abundance at the end of helium burning also play a role (see e.g. Chieffi and Limongi 2013).

6.5.1 *Advanced Phases, Final Masses and Masses of Carbon-Oxygen Cores*

In Fig. 6.15, the structure evolution diagrams are drawn as a function of the log of the time left until the last model calculated (as opposed to age in Fig. 6.4). This choice of x-axis allows one to see the evolution of the structure during the advanced stages. In the *left* panel, we can see that, at solar metallicity, VMS have an advanced evolution identical to lower mass stars (see e.g. Fig. 12 in Hirschi et al. 2004a) with a radiative core C-burning followed by a large convective C-burning shell, radiative neon burning and convective oxygen and silicon burning stages. All the solar metallicity models will eventually undergo core collapse after going through the usual advanced burning stages. As presented in Table 6.2 (column 9), the central mass fraction of ^{12}C is very low in all VMS models and is anti-correlated with the total mass at the end of helium burning (column 6): the higher the total mass, the lower the central ^{12}C mass fraction. This is due to the higher temperature in more massive cores leading to a more efficient $^{12}\mathrm{C}(\alpha,\gamma)^{16}\mathrm{O}$ relative to 3α.

The similarities between VMS and lower mass stars at solar metallicity during the advanced stages can also be seen in the central temperature versus central density diagram (see Fig. 6.16). Even the evolution of the 500 $M_\odot$ rotating model is close to that of the 60 $M_\odot$ model. The non-rotating models lose less mass as described above and thus their evolutionary track is higher (see e.g. the track for the non-rotating 150 $M_\odot$ model in Fig. 6.16). Non-rotating models nevertheless stay clear of the pair-instability region ($\Gamma < 4/3$, where Γ is the adiabatic index) in the centre.

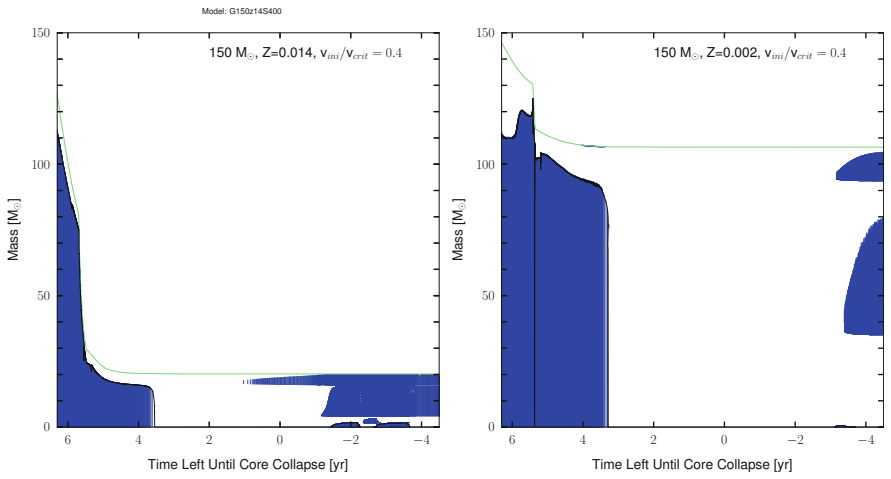

Fig. 6.15 Structure evolution diagram for rotating 150 $M_\odot$ at solar and SMC metallicities as a function of the log of the time left until the last model. The *blue zones* represent the convective regions and the *top solid line* the total mass

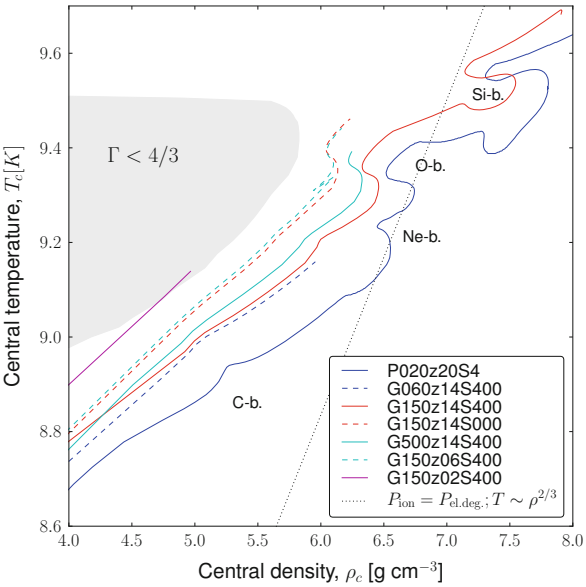

Fig. 6.16 Evolution of the central temperature T_c versus central density ρ_c for the rotating 20 (from Hirschi et al. 2004a), 60 (from Ekström et al. 2012), 150 and 500 $M_\odot$ models and non-rotating 150 $M_\odot$ model at solar metallicity as well as the rotating 150 $M_\odot$ model at SMC metallicity. The *gray shaded area* is the pair-creation instability region ($\Gamma < 4/3$, where Γ is the adiabatic index). The *additional dotted line* corresponds to the limit between non-degenerate and degenerate electron gas

The situation is quite different at SMC metallicity (see Fig. 6.15, *right* panel). Mass loss is weaker and thus the CO core is very large (93.5 $M_\odot$ for this 150 $M_\odot$ model). Such a large core starts the advanced stages in a similar way: radiative core C-burning followed by a large convective C-burning shell and radiative neon burning. The evolution starts to diverge from this point onwards. As can be seen in T_c vs ρ_c plot, the SMC 150 $M_\odot$ model enters the pair-instability region. These models will thus have a different final fate than those at solar metallicity (see below).

Figure 6.17 (see also Table 6.3) shows the final masses of VMS as a function of the initial masses. All models at solar Z, rotating or not, end with a small fraction of their initial mass due to the strong mass loss they experience. Rotation enhances mass loss by allowing the star to enter the WR phase earlier during the MS (see *top* panels of Fig. 6.4) and the final mass of non-rotating models is generally higher than that of rotating models. At low metallicities, due to the metallicity dependence of radiatively-driven stellar winds in both O-type stars (Vink et al. 2001a) and WR stars (Eldridge and Vink 2006), final masses are larger.

Figure 6.18 shows how the CO core masses vary as a function of the initial mass, rotation and metallicity. The CO core ($M_{\rm CO}$) is here defined as the core mass for which the mass fraction of C+O is greater than 75 %. Since the CO core mass is so close to the total mass, the behavior is the same as for the total mass and for the same reasons. For the rotating solar metallicity models, mass loss is so strong that all models end with roughly the same CO core mass around 20 $M_\odot$. As the metallicity decreases, so does mass loss and thus the LMC and SMC models have higher final CO core masses and the CO core mass does depend on the initial mass in a monotonous way. Finally, non-rotating models lose less mass than their rotating

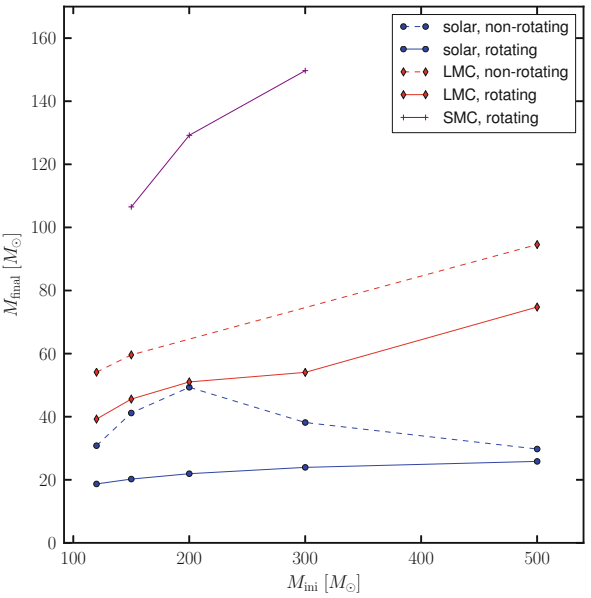

Fig. 6.17 Final mass versus initial mass for all rotating (*solid lines*) and non-rotating (*dashed line*) models

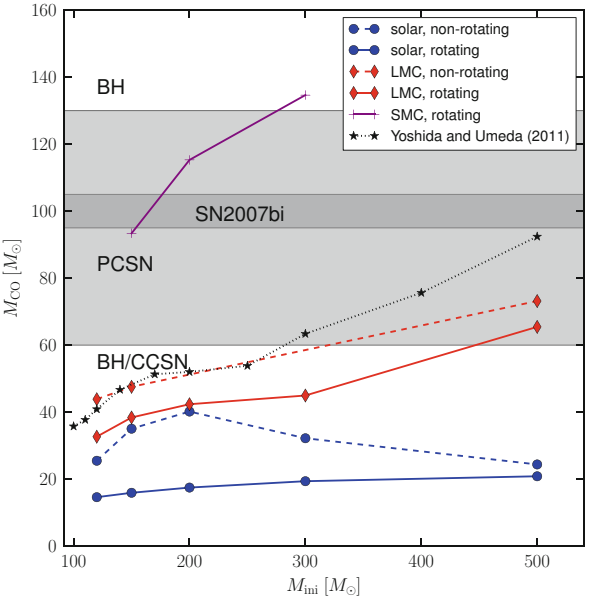

Fig. 6.18 Mass of carbon-oxygen core of all the models as a function of the initial mass. The *light grey shaded area* represents the range of M_{CO}, for which the estimated fate is a PISN. The *thin dark grey shaded area* corresponds to the estimated M_{CO} of the progenitor of SN2007bi assuming it is a PISN (see text for more details). The points linked by the *dotted black line* are from the models of Yoshida and Umeda (2011) at $Z = 0.004$, case A

counterpart since they enter the WR phase later and also have less hot surface. Simulations at $Z = 0.004$ from Yoshida and Umeda (2011) (case A) are also plotted in Fig. 6.18. The CO core masses they obtain are consistently slightly larger than for the LMC ($Z = 0.006$) models.

6.5.2 Do VMS Produce PISNe?

As mentioned above, the core masses, especially the CO core masses, can be used to estimate whether or not models produce a Pair Instability SuperNova (PISN) by using the results of previous studies, which follow the explosion of such massive cores and knowing that VMS with the same CO core masses have similar core evolution from carbon burning onwards. Heger and Woosley (2002) calculated a grid of models and found that stars with helium cores (M_α) between 64 and 133 $M_\odot$ produce PISNe and that stars with more massive M_α will collapse to a BH without explosion, confirming the results of previous studies, such as Bond et al. (1984). The independent results of Chatzopoulos and Wheeler (2012) also confirm the CO core mass range that produce PISNe.

PISNe occur when very massive stars (VMS) experience an instability in their core during the neon/oxygen burning stage due to the creation of electron-positron pairs out of two photons. The creation of pairs in their oxygen-rich core softens the equation of state, leading to further contraction. This runaway collapse is predicted to produce a very powerful explosion, in excess of 10^{53} erg, disrupting the entire star and leaving no remnant (Bond et al. 1984; Fryer et al. 2001).

Heger and Woosley (2002) also find that stars with M_α between roughly 40 and 63 $M_\odot$ will undergo violent pulsations induced by the pair-instability leading to strong mass loss but which will not be sufficient to disrupt the core. Thus these stars will eventually undergo core collapse as lower mass stars. Since in our models, the CO core masses are very close to M_α (equal to the final total mass in our models, see Table 6.5), in this chapter we assume that models will produce a PISN if $60\,M_\odot \leq M_{CO} \leq 130\,M_\odot$. In Fig. 6.18, the light grey shaded region corresponds to the zone where one would expect a PISN, the dark shaded region shows the estimated range of the carbon oxygen core of the progenitor of SN2007bi (see Yusof et al. 2013, for more details).

We see in Fig. 6.18 that at solar metallicity none of the models is expected to explode as a PISN. At the metallicity of the LMC, only stars with initial masses above 450 for the rotating models and above about 300 $M_\odot$ for the non-rotating case are expected to explode as a PISN. At the SMC metallicity, the mass range for the PISN progenitors is much more favorable. Extrapolating the points obtained from our models we obtain that all stars in the mass range between about 100 $M_\odot$ and 290 $M_\odot$ could produce PISNe. Thus these models provide support for the occurrence of PISNe in the nearby (not so metal poor) universe.

Table 6.5 presents for each of the models, the initial mass ($M_{\rm ini}$), the amount of helium left in the star at the end of the calculation ($M_{\rm He}^{\rm env}$), and final total mass as well as the estimated fate in terms of the explosion type: PISN or core-collapse supernova and black hole formation with or without mass ejection (CCSN/BH). The helium core mass (M_α) is not given since it is always equal to the final total mass, all the models having lost the entire hydrogen-rich layers.

Table 6.5 Initial masses, mass content of helium in the envelope, mass of carbon-oxygen core, final mass in solar masses and fate of the models estimated from the CO core mass

	Non-rotating				Rotating			
M_{ini}	$M_{\rm He}^{\rm env}$	$M_{\rm co}$	$M_{\rm final}$	Fate	$M_{\rm He}^{\rm env}$	$M_{\rm co}$	$M_{\rm final}$	Fate
Z = 0.014								
120	0.4874	25.478	30.8	CCSN/BH	0.5147	18.414	18.7	CCSN/BH
150	0.6142	35.047	41.2	CCSN/BH	0.5053	19.942	20.2	CCSN/BH
200	0.7765	42.781	49.3	CCSN/BH	0.5101	21.601	21.9	CCSN/BH
300	0.3467	32.204	38.2	CCSN/BH	0.4974	19.468	23.9	CCSN/BH
500	0.3119	24.380	29.8	CCSN/BH	0.5675	20.993	25.8	CCSN/BH
Z = 0.006								
120	1.2289	43.851	54.2	CCSN/BH	0.5665	32.669	39.2	CCSN/BH
150	1.1041	47.562	59.7	CCSN/BH	0.7845	38.436	45.6	CCSN/BH
200	–	–	–	CCSN/BH	0.5055	42.357	51.0	CCSN/BH
300	–	–	–	CCSN/BH	0.5802	44.959	54.0	CCSN/BH
500	1.6428	92.547	94.7	PISN	0.7865	73.145	74.8	PISN
Z = 0.002								
150	–	–	–	–	2.3353	93.468	106.5	PISN
200	–	–	–	–	3.3022	124.329	129.2	PISN
300	–	–	–	–	5.5018	134.869	149.7	BH

6.5.3 *Supernova Types Produced by VMS*

Let us recall that, in VMS, convective cores are very large. It is larger than 90 % above 200 $M_{\odot}$ at the start of the evolution and even though it decreases slightly during the evolution, at the end of core H-burning, the convective core occupies more than half of the initial mass in non-rotating models and most of the star in rotating models. This has an important implication concerning the type of supernovae that these VMS will produce. Indeed, even if mass loss is not very strong in SMC models, all the models calculated have lost the entire hydrogen rich layers long before the end of helium burning. Thus the models predict that all VMS stars in the metallicity range studied will produce either a type Ib or type Ic SN but no type II.

6.5.4 *GRBs from VMS?*

The evolution of the surface velocity was described in Sect. 6.3.6. Only models at SMC retain a significant amount of rotation during their evolution (see angular momentum contained in the CO core at the end of helium burning in the last column of Table 6.2) but do they retain enough angular momentum for rotation to affect the fate of the star? The angular momentum profile of the SMC models is presented in Fig. 6.19. Note that the models presented in this section do not include the

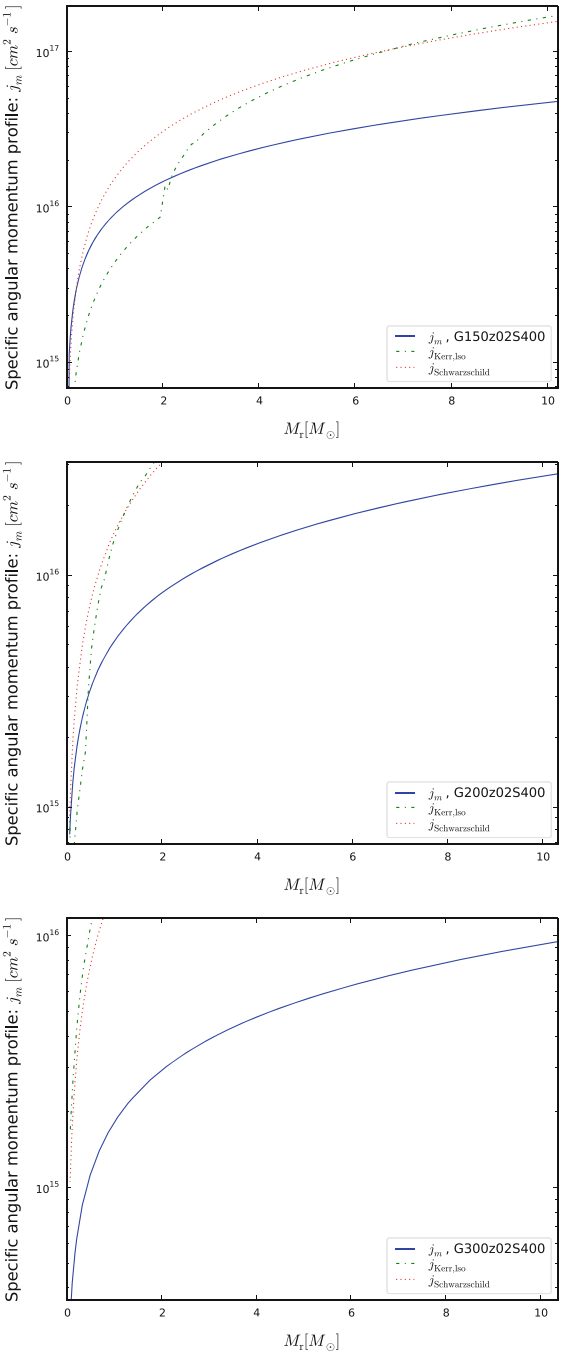

Fig. 6.19 Specific angular momentum profile, $j_{\rm m}$, as a function of the Lagrangian mass coordinate in the core of the SMC rotating 150, 200, 300 $M_\odot$ models, plotted at the end of the calculations (*solid line*). The *dash-dotted line* is $j_{\rm Kerr,lso} = r_{\rm LSO}\, c$ (Shapiro and Teukolsky 1983, p. 428), where the radius of the last stable orbit, $r_{\rm LSO}$, is given by $r_{\rm ms}$ in formula (12.7.24) from Shapiro and Teukolsky (1983, p. 362) for circular orbit in the Kerr metric. $j_{\rm Kerr,lso}$ is the minimum specific angular momentum necessary to form an accretion disc around a rotating black hole. $j_{\rm Schwarzschild} = \sqrt{12} Gm/c$ (*dotted line*) is the minimum specific angular momentum necessary for a non-rotating *black hole*, for reference

Tayler-Spruit dynamo so represent the most optimistic (highest possible) prediction concerning the angular momentum in the core of these models. Mass loss in the 300 $M_\odot$ model is too strong for the core to retain enough angular momentum for rotation to impact the death of this model. In the 200 $M_\odot$ model, and even more so in the 150 $M_\odot$ model, however, the central part of the core retain a significant amount of angular momentum that could potentially affect the death of the star. Since the role of rotation is very modest from carbon until just after the end of core silicon burning, even for extremely fast rotators (see e.g. Hirschi et al. 2005; Chieffi and Limongi 2013), we do not expect rotation to affect significantly the fate of stars that are predicted to explode as PISN during neon-oxygen burning. However, as discussed in Yoon et al. (2012, and references therein), the large angular momentum content is most interesting for the stars that just fall short of the minimum CO core mass for PISN (since fast rotation plays an important role during the early collapse Ott et al. 2004; O'Connor and Ott 2011; Chieffi and Limongi 2013). Indeed, without rotation, these stars would produce a BH following a possible pulsation pair-creation phase, whereas with rotation, these stars could produce energetic asymmetric explosions (GRBs or magnetars). Since the 150 $M_\odot$ model is predicted to explode as a PISN, we thus do not expect the models presented in this grid to produce GRBs or magnetars but such energetic asymmetric explosions are likely to take place in lower mass and lower metallicity stars (see Hirschi et al. 2005; Yoon and Langer 2005; Woosley and Heger 2006).

Yoon et al. (2012) calculated a grid of zero-metallicity rotating stars, including the Tayler-Spruit dynamo for the interaction between rotation and magnetic fields. They find that fast rotating stars with an initial mass below about 200 $M_\odot$ retain enough angular momentum in their cores in order to produce a collapsar ($j > j_{Kerr,lso}$ Woosley 1993) or a magnetar (see e.g. Wheeler et al. 2000; Burrows et al. 2007; Dessart et al. 2012). Thus some VMS that do not produce PISNe might produce GRBs instead.

6.6 The Final Chemical Structure and Contribution to Galactic Chemical Evolution

Figure 6.20 shows the chemical structure at the last time steps calculated, which is the end of the carbon burning phase in the case of the 40 $M_\odot$, and the end of the core oxygen-burning phase in the case of the 150 and 500 $M_\odot$ models. A few interesting points come out from considering this figure. First, in all cases, some helium is still present in the outer layers. Depending on how the final stellar explosion occurs, this helium may or may not be apparent in the spectrum, as discussed in Yusof et al. (2013). Second, just below the He-burning shell, products of the core He-burning, not affected by further carbon burning are apparent. This zone extends between about 4 and 10 $M_\odot$ in the 40 $M_\odot$ model, between about 32 and 35 $M_\odot$ in the 150 $M_\odot$ model and in a tiny region centered around 24 $M_\odot$

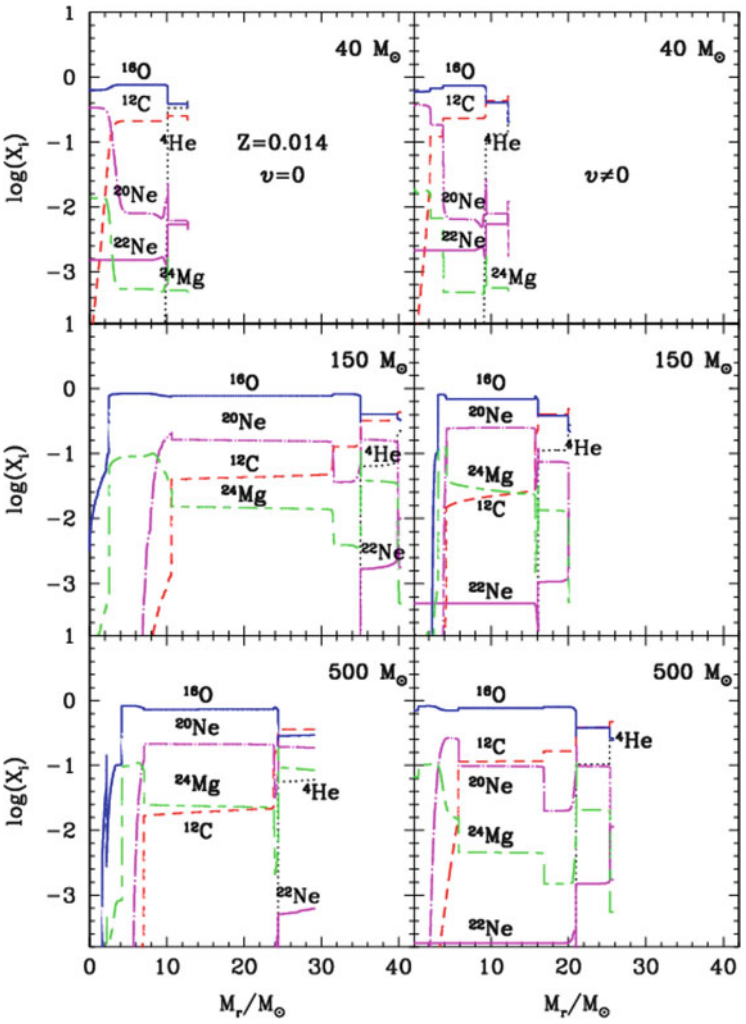

Fig. 6.20 Chemical structure of 40, 150 and 500 $M_{\odot}$ non-rotating (*left*) and rotating (*right*) models at Z = 0.014 at the end of the calculations. Note that the rotating 500 M model is shown at an earlier evolutionary stage than the corresponding non-rotating model

in the 500 $M_{\odot}$ model. We therefore see that this zone decreases in importance when the initial mass increases. Interestingly, the chemical composition in this zone present striking differences if we compare for instance the 40 $M_{\odot}$ and the 500 $M_{\odot}$ model. We can see that the abundance of ^{20}Ne is much higher in the more massive model. This comes from the fact that in more massive stars, due to higher central temperatures during the core He-burning phase the reaction ^{16}O(α, γ)^{20}Ne is more active, building thus more ^{20}Ne. Note that ^{24}Mg is also more abundant, which is natural since the reaction ^{20}Ne(α, γ)^{24}Mg reaction will also be somewhat active in

VMS for the same reasons. While in the case of the 150 $M_\odot$, due to the mass loss history, the ^{20}Ne and ^{24}Mg-rich layers are not uncovered, they are uncovered in the 500 $M_\odot$ model. This implies that strong overabundances of these two isotopes at the surface of WC stars can be taken as a signature for an initially very massive stars as the progenitor of that WC star. It also means that, contrary to what occurs at the surface of WC stars originating from lower initial mass stars, neon is no longer present mainly in the form of ^{22}Ne (and thus be a measure of the initial CNO content since resulting from the transformation of nitrogen produced by CNO burning during the H-burning phase) but will mainly be present in the form of ^{20}Ne.

Rotation does not change much this picture (see right panel of Fig. 6.20), except that, due to different mass loss histories, the rotating models lose much more mass and end their evolution with smaller cores. This is particularly striking for the 150 $M_\odot$ model. Qualitatively the situation is not much different at lower metallicities.

As stars in the mass range 50–100 $M_\odot$ (see e.g. Meynet and Maeder 2005; Chieffi and Limongi 2013), VMS eject copious amount of H-burning products through their stellar winds and to a lesser extent He-burning products. The potential difference between VMS and stars in the mass range 50–100 $M_\odot$ is how they explode (or not) at the end of their life, which is discussed in detail in the next chapter. If they collapse to a black hole the contribution from the supernova will be negligible whereas if they explode as PISNe they will produce large amounts of iron and other heavy elements.

Do VMS contribute to the chemical enrichment of galaxies or are VMS so rare that whatever their evolution, their impact on energy and mass outputs will anyway be very low? Considering a Salpeter IMF, the number of stars with masses between 120 and 500 $M_\odot$ corresponds to only about 2 % of the total number of stars with masses between 8 and 500 $M_\odot$. So they are indeed only very few! On the other hand, one explosion can release a great amount of energy and mass into the interstellar medium. Typically a 200 $M_\odot$ star releases about ten times more mass than a 20 $M_\odot$ star. If we roughly suppose that for hundred 20 $M_\odot$ stars there are only two 200 $M_\odot$ star, this means that the 200 $M_\odot$ stars contribute to the release of mass at a level corresponding to about 20 % of the release of mass by 20 $M_\odot$, which is by far not negligible. Of course this is a rough estimate but, as a rule of thumb we can say that any quantity released by a VMS $\sim$ tenfold intensity compared to that of a typical, 20 $M_\odot$ star will make a non-negligible difference in the overall budget of this quantity at the level of a galaxy. For instance, the high bolometric luminosities, stellar temperatures and mass loss rates of VMS imply that they will contribute significantly to the radiative and mechanical feedback from stars in high mass clusters at ages prior to the first supernovae (Crowther et al. 2010). Core-collapse SNe produce of the order of 0.05 $M_\odot$ (ejected masses) of iron, 1 $M_\odot$ of each of the $\alpha-$elements. According to the production factors in Table 6.4 in Heger and Woosley (2002), PISN produce up to 40 $M_\odot$ of iron, of the order of 30 $M_\odot$ of oxygen and silicon and of the order of 5–10 $M_\odot$ of the other $\alpha-$elements. Considering that PISN may occur up to SMC metallicity and represent 2 % of SNe at a given metallicity, their contribution to the chemical enrichment of galaxies may

be significant, especially in the case of iron, oxygen and silicon. If the IMF is top heavy at low metallicities, the impact of VMSs would be even larger.

Summary and Conclusion

In this chapter, we have discussed the evolution of very massive stars based on stellar evolution models at various metallicities. The main properties of VMS are the following:

- VMS possess very large convective cores during the MS phase. Typically, in a 200 $M_{\odot}$ model on the ZAMS the convective core extends over more than 90 % of the total mass.
- Since the mass-luminosity relation flattens above 20 $M_{\odot}$, VMS have lifetimes that are not very sensitive to their initial mass and range between 2 and 3.5 million years.
- Even in models with no rotation, due to the importance of the convective core, VMS evolve nearly chemically homogeneously.
- Most of the very massive stars (all at solar Z) remain in blue regions of the HR diagram and do not go through a luminous blue variable phase.
- They all enter into the WR phase and their typical evolution is Of – WNL-WNE - WC/WO.
- Due to increasing mass loss rates with the mass, very different initial mass stars end with similar final masses. As a consequence very different initial masses may during some of their evolutionary phases occupy very similar positions in the HRD.
- A significant proportion of the total stellar lifetimes of VMS is spent in the WR phase (about a third).
- A WC star with high Ne (^{20}Ne) and Mg (^{24}Mg) abundances at the surface has necessarily a VMS as progenitor.
- At solar metallicity VMS are not expected to explode as PISNe because mass loss rates are too high.
- Whether or not some VMS models retain enough mass to produce a PISN at low metallicity is strongly dependent on mass loss. As discussed above, models that retain enough mass at SMC metallicity (and below) also approach very closely the Eddington limit after helium burning and this might trigger a strong enough mass loss in order to prevent any VMS from producing a PISN.
- Most VMS lose the entire hydrogen rich layers long before the end of helium burning. Thus most VMS stars near solar metallicity are expected to produce either a type Ib or type Ic SN but no type II.
- Models near solar metallicity are not expected to produce GRBs or magnetars. The reason for that is that either they lose too much angular momentum by mass loss or they avoid the formation of a neutron star or

(continued)

BH because they explode as PISN. Lower mass stars at low metallicities ($Z \lesssim 0.002$), however, may retain enough angular momentum as in metal free stars (see Yoon et al. 2012; Chatzopoulos and Wheeler 2012) for rotation (and magnetic fields) to play a significant role in their explosion.

Even though VMS are rare, their extreme luminosities and mass loss will still contribute significantly to the light and chemistry budget of their host galaxies. And although many VMS will die quietly and form a black hole, some VMS may die as PISNe or GRBs. Thus the extreme properties of VMS compensate for their rarity and they are worth studying and considering in stellar population and galactic chemical evolution studies. As discussed above, the main uncertainty that strongly affects their evolution and their fate is the uncertainty in mass loss, especially for stars near the Eddington limit. Thus, although the discussions and conclusions presented in this chapter will remain qualitatively valid, quantitative results will change as our knowledge of mass loss in these extreme stars improves.

Acknowledgements The author thanks his collaborators at the University of Keele (C. Georgy), Geneva (G. Meynet, A. Maeder and Sylvia Ekström) and Malaysia (N. Yusof and H. Kassim) for their significant contributions to the results presented in this chapter. R. Hirschi acknowledges support from the World Premier International Research Center Initiative (WPI Initiative), MEXT, Japan and from the Eurogenesis EUROCORE programme. The research leading to these results has received funding from the European Research Council under the European Union's Seventh Framework Programme (FP/2007–2013)/ERC Grant Agreement n. 306901.

References

Abel, T., Bryan, G. L., & Norman, M. L. (2002). *Science, 295*, 93
Bennett, M. E., Hirschi, R., Pignatari, M., et al. (2012). *Monthy Notices of the Royal Astronomical Society, 420*, 3047
Bond, J. R., Arnett, W. D., & Carr, B. J. (1984). *Astrophysics Journal, 280*, 825
Brüggen, M., & Hillebrandt, W. (2001). *Monthy Notices of the Royal Astronomical Society, 323*, 56
Braithwaite, J. (2006). *Astronomy and Astrophysics, 449*, 451
Bromm, V., Coppi, P. S., & Larson, R. B. (1999). *Astrophysics Journal Letters, 527*, L5
Burrows, A., Dessart, L., Livne, E., Ott, C. D., & Murphy, J. (2007). *Astrophysics Journal, 664*, 416
Canuto, V. M. (2002). *Astronomy and Astrophysics, 384*, 1119
Chaboyer, B., & Zahn, J.-P. (1992). *Astronomy and Astrophysics, 253*, 173
Chatzopoulos, E., & Wheeler, J. C. (2012). *Astrophysics Journal, 748*, 42
Chieffi, A., & Limongi, M. (2013). *Astrophysics Journal, 764*, 21
Chieffi, A., Limongi, M., & Straniero, O. (1998). *Astrophysics Journal, 502*, 737
Christlieb, N., Bessell, M. S., Beers, T. C., et al. (2002). *Nature, 419*, 904

Crowther, P. A. (2001). In D. Vanbeveren (Ed.), *Astrophysics and Space Science Library* (The Influence of Binaries on stellar population studies, Vol. 264, p. 215). ISBN: 0792371046, Springer.
Crowther, P. A., Hirschi, R., Walborn, N., & N., Y. (2012). In L. Drissen, C. Robert, N. St-Louis, & A. Moffat (Eds.) *Four decades of research on massive stars* (Astronomical Society of the Pacific, San Fransisco, conference series)
Crowther, P. A., Schnurr, O., Hirschi, R., et al. (2010). *Monthy Notices of the Royal Astronomical Society, 408*, 731
de Jager, C., Nieuwenhuijzen, H., & van der Hucht, K. A. (1988a). *Astronomy and Astrophysics Supplement, 72*, 259
de Jager, C., Nieuwenhuijzen, H., & van der Hucht, K. A. (1988b). *Astronomy and Astrophysics Supplement, 72*, 259
Dessart, L., O'Connor, E., & Ott, C. D. (2012). *Astrophysics Journal, 754*, 76
Dessart, L., Waldman, R., Livne, E., Hillier, D. J., & Blondin, S. (2013). *Monthy Notices of the Royal Astronomical Society, 428*, 3227
Eggenberger, P., Meynet, G., Maeder, A., et al. (2007). *Astrophysics and Space Science, 263*
Ekström, S., Georgy, C., Eggenberger, P., et al. (2012). *Astronomy and Astrophysics, 537*, A146
Ekström, S., Meynet, G., Chiappini, C., Hirschi, R., & Maeder, A. (2008). *Astronomy and Astrophysics, 489*, 685
Eldridge, J. J., Izzard, R. G., & Tout, C. A. (2008). *Monthy Notices of the Royal Astronomical Society, 384*, 1109
Eldridge, J. J., & Vink, J. S. (2006). *Astronomy and Astrophysics, 452*, 295
Figer, D. F. (2005). *Nature, 434*, 192
Frebel, A., Aoki, W., & Christlieb, N., e. a. (2005). *Nature, 434*, 871
Fricke, K. (1968). *Zeitschrift fur Astrophysics, 68*, 317
Frischknecht, U., Hirschi, R., Meynet, G., et al. (2010). *Astronomy and Astrophysics, 522*, A39
Fryer, C. L., Woosley, S. E., & Heger, A. (2001). *Astrophysics Journal, 550*, 372
Georgy, C., Ekström, S., Meynet, G., et al. (2012). *Astronomy and Astrophysics, 542*, A29
Georgy, C., Ekström, S., Eggenberger, P., et al. (2013). *Astronomy and Astrophysics, 558*, A103
Georgy, C., Meynet, G., & Maeder, A. (2011) *Astronomy and Astrophysics, 527*, A52
Goldreich, P., & Schubert, G. (1967). *Astrophysics Journal, 150*, 571
Gräfener, G., & Hamann, W.-R. (2008). *Astronomy and Astrophysics, 482*, 945
Greif, T. H., Glover, S. C. O., Bromm, V., & Klessen, R. S. (2010). *Astrophysics Journal, 716*, 510
Hamann, W.-R., Gräfener, G., & Liermann, A. (2006). *Astronomy and Astrophysics, 457*, 1015
Heger, A., Langer, N., & Woosley, S. E. (2000). *Astrophysics Journal, 528*, 368
Heger, A. & Woosley, S. E. (2002). *Astrophysics Journal, 567*, 532
Hirschi, R. (2007). *Astronomy and Astrophysics, 461*, 571
Hirschi, R. & Maeder, A. (2010). *Astronomy and Astrophysics, 519*, A16
Hirschi, R., Meynet, G., & Maeder, A. (2004a). *Astronomy and Astrophysics, 425*, 649
Hirschi, R., Meynet, G., & Maeder, A. (2004b). *Astronomy and Astrophysics, 425*, 649
Hirschi, R., Meynet, G., & Maeder, A. (2005). *Astronomy and Astrophysics, 443*, 581
Kippenhahn, R., & Weigert, A. (1990). *Stellar structure and evolution*. Berlin/New York, Springer.
Kippenhahn, R., Weigert, A., & Hofmeister, E. (1967). In B. Alder, S. Fernbach, & M. Rotenberg (Eds.), *Methods in Computational Physics* (Vol. 7). New York: Academic Press.
Knobloch, E., & Spruit, H. C. (1983). *Astronomy and Astrophysics, 125*, 59
Krtička, J., Owocki, S. P., & Meynet, G. (2011). *Astronomy and Astrophysics, 527*, A84
Langer, N. (2012). *ARA&A, 50*, 107
Maeder, A. (1980). *Astronomy and Astrophysics, 92*, 101
Maeder, A. (1997). *Astronomy and Astrophysics, 321*, 134
Maeder, A. (2003). *Astronomy and Astrophysics, 399*, 263
Maeder, A. (2009). *Physics, formation and evolution of rotating stars*. Berlin/Heidelberg, Springer.
Maeder, A., Georgy, C., Meynet, G., & Ekström, S. (2012). *Astronomy and Astrophysics, 539*, A110
Maeder, A., & Meynet, G. (2000). *Astronomy and Astrophysics, 361*, 159

Meynet, G., & Maeder, A. (2002). *Astronomy and Astrophysics, 390*, 561
Maeder, A., & Meynet, G. (2005). *Astronomy and Astrophysics, 440*, 1041
Maeder, A., & Meynet, G. (2012). *Reviews of Modern Physics, 84*, 25
Maeder, A., & Zahn, J. (1998). *Astronomy and Astrophysics, 334*, 1000
Meynet, G., & Maeder, A. (1997). *Astronomy and Astrophysics, 321*, 465
Meynet, G., & Maeder, A. (2005). *Astronomy and Astrophysics, 429*, 581
Muijres, L. E., de Koter, A., Vink, J. S., et al. (2011). *Astronomy and Astrophysics, 526*, A32
Nugis, T., & Lamers, H. J. G. L. M. (2000a). *Astronomy and Astrophysics, 360*, 227
Nugis, T., & Lamers, H. J. G. L. M. (2000b). *Astronomy and Astrophysics, 360*, 227
O'Connor, E., & Ott, C. D. (2011). *Astrophysics Journal, 730*, 70
Oey, M. S., & Clarke, C. J. (2005). *Astrophysics Journal Letters, 620*, L43
Ott, C. D., Burrows, A., Livne, E., & Walder, R. (2004). *Astrophysics Journal, 600*, 834
Paxton, B., Bildsten, L., Dotter, A., et al. (2011). *Astrophysics Journal Supplement Series, 192*, 3
Potter, A. T., Chitre, S. M., & Tout, C. A. (2012). *Monthy Notices of the Royal Astronomical Society, 424*, 2358
Salpeter, E. E. (1955). *Astrophysics Journal, 121*, 161
Sander, A., Hamann, W.-R., & Todt, H. (2012). *Astronomy and Astrophysics, 540*, A144
Schneider, F. R. N., Izzard, R. G., de Mink, S. E., et al. (2014). *Astrophysics Journal, 780*, 117
Shapiro, S. L. & Teukolsky, S. A. (1983). *Black Holes, White Dwarfs and Neutron Stars: The Physics of Compact Objects* (Research supported by the National Science Foundation, p. 663) New York: Wiley-Interscience. http://eu.wiley.com/WileyCDA/WileyTitle/productCd-0471873160.html
Spruit, H. C. (2002). *Astronomy and Astrophysics, 381*, 923
Stacy, A., Greif, T. H., & Bromm, V. (2010). *Monthy Notices of the Royal Astronomical Society, 403*, 45
Sylvester, R. J., Skinner, C. J., & Barlow, M. J. (1998). *Monthy Notices of the Royal Astronomical Society, 301*, 1083
Umeda, H., & Nomoto, K. (2002). *Astrophysics Journal, 565*, 385
van Loon, J. T., Groenewegen, M. A. T., de Koter, A., et al. (1999). *Astronomy and Astrophysics, 351*, 559
Vink, J. S., de Koter, A., & Lamers, H. J. G. L. M. (2001a). *Astronomy and Astrophysics, 369*, 574
Vink, J. S., de Koter, A., & Lamers, H. J. G. L. M. (2001b). *Astronomy and Astrophysics, 369*, 574
Vink, J. S., Gräfener, G., & Harries, T. J. (2011a). *Astronomy and Astrophysics, 536*, L10
Vink, J. S., Muijres, L. E., Anthonisse, B., de Koter, A., Gräfener, G., Langer, N., (2011b). Wind modelling of very massive stars up to 300 solar masses. *Astronomy and Astrophysics, 531*, A132. doi: 10.1051/0004-6361/201116614. Provided by the SAO/NASA Astrophysics Data System http://adsabs.harvard.edu/abs/2011A26A...531A.132V
von Zeipel, H. (1924). *Monthy Notices of the Royal Astronomical Society, 84*, 665
Walder, R., Folini, D., & Meynet, G. (2011). *Space Science Reviews, 125*
Wheeler, J. C., Yi, I., Höflich, P., & Wang, L. (2000). *Astrophysics Journal, 537*, 810
Woosley, S. E. (1993). *Astrophysics Journal, 405*, 273
Woosley, S. E. & Heger, A. (2006). *Astrophysics Journal, 637*, 914
Yoon, S.-C., Dierks, A., & Langer, N. (2012). *Astronomy and Astrophysics, 542*, A113
Yoon, S.-C. & Langer, N. (2005). *Astronomy and Astrophysics, 443*, 643
Yoon, S.-C., Langer, N., & Norman, C. (2006). *Astronomy and Astrophysics, 460*, 199
Yoshida, T. & Umeda, H. (2011). *Monthy Notices of the Royal Astronomical Society, 412*, L78
Yusof, N., Hirschi, R., Meynet, G., et al. (2013). *Monthy Notices of the Royal Astronomical Society, 433*, 1114
Zahn, J., Brun, A. S., & Mathis, S. (2007). *Astronomy and Astrophysics, 474*, 145
Zahn, J.-P. (1992). *Astronomy and Astrophysics, 265*, 115